ADVANCED MATERIALS
www.advmat.de

Plasmon-Enhanced Photoelectrochemical Water Splitting for Efficient Renewable Energy Storage

Luca Mascaretti, Aveek Dutta, Štěpán Kment, Vladimir M. Shalaev, Alexandra Boltasseva, Radek Zbořil,* and Alberto Naldoni**

Photoelectrochemical (PEC) water splitting is a promising approach for producing hydrogen without greenhouse gas emissions. Despite decades of unceasing efforts, the efficiency of PEC devices based on earth-abundant semiconductors is still limited by their low light absorption, low charge mobility, high charge-carrier recombination, and reduced diffusion length. Plasmonics has recently emerged as an effective approach for overcoming these limitations, although a full understanding of the involved physical mechanisms remains elusive. Here, the reported plasmonic effects are outlined, such as resonant energy transfer, scattering, hot electron injection, guided modes, and photonic effects, as well as the less investigated catalytic and thermal effects used in PEC water splitting. In each section, the fundamentals are reviewed and the most representative examples are discussed, illustrating possible future developments for achieving improved efficiency of plasmonic photoelectrodes.

1. Introduction

The conversion of solar energy into chemical fuels represents the most promising route for achieving a sustainable energy economy. A photoelectrochemical (PEC) cell for water splitting[1] uses semiconductors to split water into pure hydrogen (H_2) and oxygen (O_2). H_2 is an ideal energy vector for transportation, energy storage, and the production of electricity at zero-carbon emission. These properties are attributed to its very high energy density (120 MJ kg^{-1}), which is ≈2.5 times higher than that of traditional fossil fuels such as methane, gasoline, and diesel. H_2 is also essential for ammonia production and as a feedstock for the production of liquid fuels from CO_2 reduction.

Dr. L. Mascaretti, Dr. Š. Kment, Prof. R. Zbořil, Dr. A. Naldoni
Regional Centre of Advanced Technologies and Materials
Faculty of Science
Palacký University Olomouc
Šlechtitelů 27, 783 71 Olomouc, Czech Republic
E-mail: radek.zboril@upol.cz; alberto.naldoni@upol.cz
A. Dutta, Prof. V. M. Shalaev, Prof. A. Boltasseva
School of Electrical & Computer Engineering
and Birck Nanotechnology Center
Purdue University
West Lafayette, IN 47907, USA
E-mail: aeb@purdue.edu
The ORCID identification number(s) for the author(s) of this article can be found under https://doi.org/10.1002/adma.201805513.

DOI: 10.1002/adma.201805513

The overall solar water splitting reaction is endothermic ($\Delta E = 1.23$ V) and consists of two half reactions, i.e., the hydrogen evolution reaction (HER) and the oxygen evolution reaction (OER):

$$2H_2O \rightarrow 2H_2 + O_2 \quad (1)$$

$$4H^+ + 4e^- \rightarrow 2H_2 \quad (\mathrm{HER}, E^0_{\mathrm{red}} = 0.0 \text{ V vs RHE}) \quad (2)$$

$$2H_2O + 4h^+ \rightarrow O_2 + 4H^+ \quad (\mathrm{OER}, E^0_{\mathrm{ox}} = 1.23 \text{ V vs RHE}) \quad (3)$$

where the redox potentials are referred versus the reversible hydrogen electrode (RHE).

In a conventional PEC device, the reduction (HER) and oxidation (OER) half-reactions occur on the surface of the cathode and anode, respectively, in an aqueous electrolyte, which closes the current circuit between the electrodes. The electrochemical behavior of the photoelectrodes is dictated by their electronic properties and type of mobility, such that n-type semiconductors operate as photoanodes and accordingly p-type as photocathodes.[1–4]

Once the photoelectrode is in contact with an electrolyte, a space-charge (depletion) layer is formed at the semiconductor/liquid junction (SCLJ). Photoexcited electron–hole pairs are generated during light illumination and become separated due to the space-charge field (i.e., the photovoltage). In the case of a photoanode (photocathode), this electric field drives holes (electrons) toward the interface of the solid electrode and the liquid electrolyte, where they oxidize (reduce) water, thereby generating O_2 (H_2). In contrast, the photogenerated electrons (holes) are transferred via the external circuit to a metallic cathode (anode), where they reduce (oxidize) water, thereby generating H_2 (O_2). This category of PEC cells is referred to as Schottky-type configuration (**Figure 1**a) and is currently the most frequently investigated configuration. With this architecture, semiconductor candidates for the cathodic or the anodic half-reaction can be separately studied, and eventually coupled either together or with a solar cell to provide the necessary photovoltage to drive water splitting without the application of an external bias voltage.

Materials used as photoelectrodes must exhibit a bandgap (E_g) ≥ 1.23 eV, i.e., higher than the thermodynamic redox potential for overall water splitting, while featuring conduction

band (E_{CB}) and valence band (E_{VB}) edges that straddle H_2O redox potentials E^0_{red} and E^0_{ox}, respectively. Furthermore, candidate materials must be low cost, and exhibit high chemical stability, high carrier mobility, high carrier lifetime, and rapid interfacial charge transfer. The CB and VB of the semiconductor may have suitable energies, but unavoidable potential losses and kinetic overpotentials imply that an actual energy of 1.6–2.4 eV is required to sustain the overall water splitting. Owing to these stringent thermodynamic and kinetic requirements, a single semiconductor that yields a high-efficiency overall reaction remains elusive. Moreover, in contrast to materials for photovoltaics (PV), PEC electrodes (especially photoanodes) undergo severe photocorrosion, due to charge carriers with high oxidation potential at the semiconductor surface.

A recent technoeconomic study performed by the US Department of Energy has set the target cost of H_2 from PEC water splitting as 2 \$ kg^{-1}, which will enable competitiveness with the existing technologies.[5] This translates to the development of devices with solar-to-hydrogen (STH) efficiency of 10%, for a return on the investment. The STH efficiency reads

$$\mathrm{STH} = \left[\frac{|J_{ph} \cdot \Delta E \cdot \eta_F|}{P_{light}}\right]_{AM1.5G} \quad (4)$$

where J_{ph} is the photocurrent (in mA cm^{-2}), η_F is the faradaic efficiency for hydrogen production (100% if all the photocurrent leads to O_2 and H_2 without side products), and P_{light} is the power of incident light (100 mW cm^{-2} for AM 1.5G illumination). Equation (4) is only valid if one confirms stoichiometric gas evolution (H_2 and O_2) in the absence of any sacrificial donors or acceptors in a two-electrode PEC cell.

Owing to the use of photoelectrodes based on Si and III–V semiconductors,[5] record STH efficiency values (10% for Si[6] and 19.3% for GaAs/GaInAs/GaInP/AlInP dual-junction tandem PEC/PV)[7] have been realized, although these materials exhibit low stability (maximum 100 h for Si).[8,9] These semiconductors are characterized by large charge mobility, high light absorption, and optimal E_g, but are associated with high manufacturing costs. Moreover, their poor stability in PEC conditions prevents long-term device durability.

Furthermore, earth-abundant metal oxides (Figure 1b), such as TiO_2, α-Fe_2O_3, WO_3, and $BiVO_4$ exhibit outstanding PEC long-term stability and promising efficiency (7.7% for a dual α-Fe_2O_3/$BiVO_4$ photoanode),[10–14] representing a promising option for PEC cells. They are characterized (in general) by low processing cost, high stability (even in harsh environments), low light absorption, low minority carrier diffusion length, and high recombination.[15]

In this scenario, plasmonics has emerged as a powerful approach to overcome the general drawbacks of earth-abundant materials ensuring the possibility to be integrated in the various components forming a PEC water splitting device and finally enhance its performance, as already pointed out in several reviews.[16–22]

To the best of our knowledge, this review differs from the previous ones as it provides a comprehensive theoretical framework for the various phenomena related to surface plasmons and it describes, one by one, their exploitation in PEC water splitting experiments. We start with a basic introduction on the physics of plasmons and a description of the interaction mechanisms between plasmonic and semiconductor materials (Section 2). The optical properties of both traditional and alternative plasmonic materials employed for PEC water splitting are discussed in parallel to device costs, as well as material integration and

Alexandra Boltasseva is a Professor at the School of Electrical and Computer Engineering at Purdue University. She received her Ph.D. in electrical engineering at Technical University of Denmark in 2004. Her research focuses on nanophotonics, optical materials, plasmonics, metamaterials, and quantum plasmonics.

Radek Zbořil (*1973) received his Ph.D. degree at the Palacky University in Olomouc, Czech Republic. After his doctoral studies, he spent some time at universities around the world in locations such as Tokyo, Delaware, and Johannesburg. Currently, he is a General Director of the Regional Centre of Advanced Technologies and Materials at the Palacky University in Olomouc, Czech Republic. His research interests focus on nanomaterial research for applications in catalysis, water treatment, antimicrobial technologies, medicine, energy storage, and biotechnologies.

Alberto Naldoni is co-leader of the nano-photoelectrochemistry group at the Regional Centre of Advanced Technologies and Materials of Palacký University Olomouc. He obtained his Ph.D. (2010) in chemical sciences from University of Milan before moving to the Italian National Research Council to study photocatalysis and photoelectrochemical water splitting. He spent 3 years as visiting faculty in the Nanophotonics group at the Birck Nanotechnology Center of Purdue University. His research interests focus on solar energy conversion with emphasis on plasmonics, photoelectrochemistry, and photocatalysis.

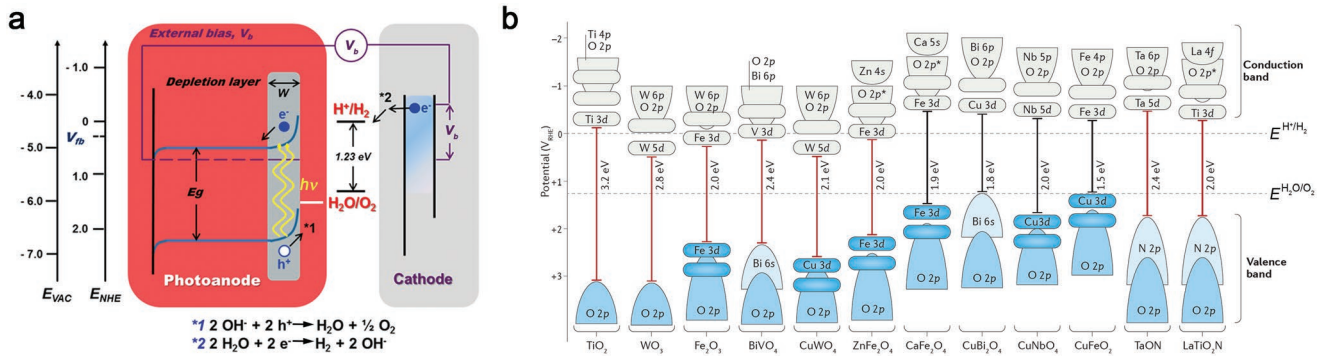

Figure 1. a) Schematic of a Schottky PEC cell showing a photoanode in contact with the electrolyte resulting in the formation of a depletion layer (width: w). The photoanode has a bandgap (E_g), a flat band potential (V_{fb}), and drives the water splitting under an applied bias (V_b). Energy scales are reported both versus vacuum (E_{VAC}) and the normal hydrogen electrode (E_{NHE}). b) Schematic showing bandgap energy (red for n-type, black for p-type) and alignment versus RHE, and the H_2O redox potentials of promising earth-abundant materials for PEC water splitting. Each representation also shows the contribution of metal cations and oxygen anions to the conduction and valence bands. Reproduced with permission.[23] Copyright 2016, Nature Publishing Group.

chemical stability. In Section 3, we present a detailed overview of all plasmonic effects that have yielded significant enhancement in PEC water splitting. In Section 4, we discuss the catalytic effects exerted by plasmonic nanostructures. Section 5 highlights examples of devices where all charges involved in chemical reactions leading to PEC water splitting are hot carriers generated inside plasmonic absorber units. With this complete set of tools, we provide the basis for the design of new plasmonic photoelectrodes with enhanced performance that enables a practical implementation of PEC technologies for renewable-energy utilization.

2. Plasmonics

2.1. Fundamentals

The optical properties of metals can be conveniently explained by treating conduction electrons as a free electron gas through the Drude model.[24] In this scenario, electrons with number density n and effective mass m^* can oscillate in response to an applied electromagnetic field, while positive ions are treated as immobile. Above the characteristic frequency, referred to as plasma frequency (ω_p), electromagnetic waves can be transmitted in the material, while at ω_p a longitudinal collective oscillation of free electrons occurs. This collective oscillation is referred to as volume plasmon (**Figure 2**a) and the corresponding frequency is given as

$$\omega_p = \sqrt{\frac{ne^2}{\varepsilon_0 m^*}} \tag{5}$$

where e is the elementary charge and ε_0 is the vacuum permittivity. Therefore, the complex relative permittivity of a conductive material can be expressed as

$$\tilde{\varepsilon}(\omega) = \varepsilon'(\omega) + i\varepsilon''(\omega) = \varepsilon_{int} - \frac{\omega_p^2}{\omega(\omega + i\Gamma)} \tag{6}$$

where $\Gamma = 1/\tau$, with τ being the mean relaxation time of conduction electrons, and ε_{int} accounts for interband transitions, which are neglected by the Drude model and occur at visible frequencies for noble metals; this term can be accounted for by including Lorentz oscillators. At the interface between a dielectric (i.e., air) and a conductor, a different type of excitation, referred to as surface plasmon polariton (SPP), can occur. A SPP consists in an electromagnetic wave propagating along the interface and evanescently confined in the perpendicular direction (Figure 2b).[25] For the dielectric, a real and positive permittivity ε_d is considered, and the metal is described by $\varepsilon'(\omega) < 0$. The propagation of the SPP along the x axis is characterized by a transverse-magnetic (TM) or p polarization and is associated with a surface charge density fluctuation. In addition, the electric field component E_z decays along the normal direction to the interface with different penetration depths in the metal (δ_m) and the dielectric (δ_d) (Figure 2b). These quantities are typically in the order of 100 nm–1 µm, and are inversely proportional to the propagation length of the SPP (i.e., 10 µm–1 mm).[26,27] The characteristic SPP frequency is given by

$$\omega_{SPP} = \frac{\omega_p}{\sqrt{1+\varepsilon_d}} \tag{7}$$

Furthermore, the so-called localized surface plasmon resonance (LSPR) may occur in the case of nanoparticles (NPs) or nanostructures (Figure 2c).[25] In contrast to SPP, the LSP is a nonpropagating excitation of conduction electrons and can be excited via simple light illumination. The SPP excitation can, however, only be observed if the momentum mismatch between the photon and SPP wave is satisfied. This can be achieved by using special techniques, such as electron impact or prism-coupling. The essential features of LSPR can be understood by considering the simple quasi-static approximation, which is valid for spherical metal NPs (with radius R) significantly smaller than the incident wavelength, i.e., $2R << \lambda$, and assumes $\varepsilon''(\omega) << 1$. In this case, the particle polarizability, α, exhibits a resonance for the Frölich condition, $\varepsilon'(\omega) = -2\varepsilon_d$, and, hence, the localized (dipole) surface plasmon frequency has the form

$$\omega_{LSPR} = \frac{\omega_p}{\sqrt{1+2\varepsilon_d}} \tag{8}$$

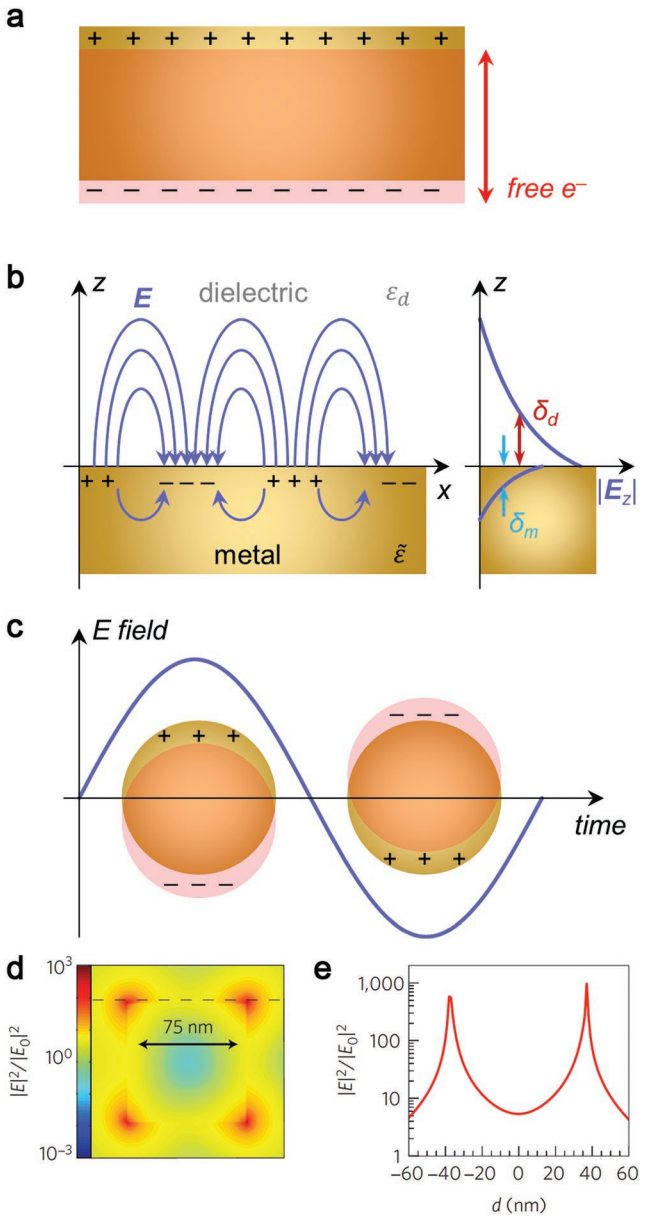

Figure 2. Schematic showing: a) volume plasmon, b) surface plasmon polariton (SPP) propagating at a metal–dielectric interface, and c) localized surface plasmon (LSP). d,e) Spatial distribution of the LSP-induced enhancement of the electric field intensity at 420 nm, determined from a finite-difference time-domain (FDTD) simulation for a 75 nm Ag nanocube. The electric field profile versus distance in (e) was calculated along the dashed line in (d). d,e) Reproduced with permission.[32] Copyright 2011, Nature Publishing Group.

which clearly shows that the resonance redshifts with increasing ε_d. The electromagnetic radiation exciting the LSPR can be either absorbed or scattered by the NP; the corresponding scattering and absorption cross sections, σ_{sca} and σ_{abs}, can be expressed as[28]

$$\sigma_{sca} = \frac{k^4}{6\pi}|\alpha|^2 = \frac{8\pi}{3}k^4R^6\left|\frac{\tilde{\varepsilon}-\varepsilon_d}{\tilde{\varepsilon}+2\varepsilon_d}\right|^2 \quad (9)$$

$$\sigma_{abs} = k\mathrm{Im}[\alpha] = 4\pi kR^3\mathrm{Im}\left[\frac{\tilde{\varepsilon}-\varepsilon_d}{\tilde{\varepsilon}+2\varepsilon_d}\right] \quad (10)$$

where k is the free space wave-vector of the electromagnetic wave. The total extinction cross-section is the sum of the former terms,

$$\sigma_{ext} = \sigma_{sca} + \sigma_{abs} \quad (11)$$

The different scaling laws for absorption (R^3) and scattering (R^6) imply the prevalence of the former for small particles and the latter for sizes larger than ≈50 nm.[29] However, at this point, the quasi-static approximation is no longer valid and the Mie theory must be considered, valid for spherical NPs of arbitrary size;[30] nonetheless, the scaling law is still valid. **Figure 3** shows an example of such calculations for Au NPs in air. An important feature of the LSPR is the electric field (***E***) enhancement, which is correlated with the proportionality between ***E*** outside the nanostructure and α.[31] This effect is particularly evident when the nanostructures exhibit sharp corners, as for polyhedral particles (Figure 2d,e). For example, an electric field enhancement of 10^3 has been calculated at the vertices of a 75 nm Ag

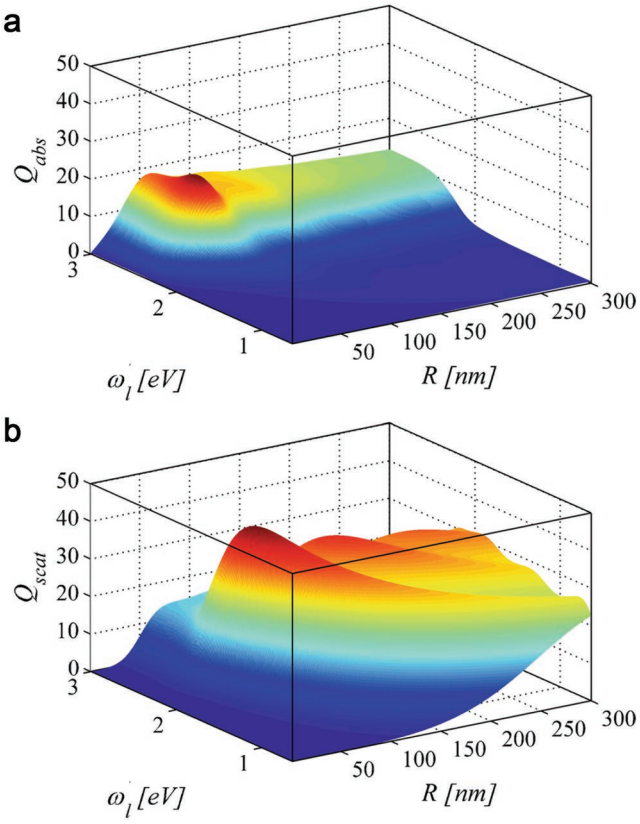

Figure 3. a,b) Efficiency of absorption $Q_{abs}(\omega,R)$ (a) and scattering $Q_{scat}(\omega,R)$ (b) of Au nanospheres as predicted by Mie theory in air. Note that $Q = \sigma/S$, where σ is either the absorption or scattering cross-section and S is the particle area. Reproduced under the terms of the CC-BY Creative Commons Attribution 4.0 International License (http://creativecommons.org/licenses/by/4.0/).[33] Copyright 2015, The Authors, published by Springer.

nanocube, which decreases exponentially within a few tens of nm from the surface.[32] Moreover, higher field intensities (10^5) can be observed in the gaps between nanostructures spaced at a few nanometers; these are referred to as "hot spots" and are particularly interesting for various applications.

The lifetime of a LSP oscillation can be expressed as the plasmon dephasing time, T_2, which in turn can be determined by experimentally measuring the damping constant Γ (in energy units) and using the relation[34]

$$T_2 = 2\hbar/\Gamma \tag{12}$$

Accordingly, **Figure 4** shows the time evolution of LSPR and the related decay processes for a plasmonic nanostructure coupled with a semiconductor, clarifying the important mechanisms in PEC water splitting experiments.

a) The LSPR decays after 1–20 fs:[34,35] T_2 values of 5–8 and 1.4 fs were obtained, respectively, for small (15–20 nm diameter) and "big" (150 nm) Au NPs,[34,35] while 100 nm long nanorods exhibited dephasing times up to 18 fs.[35] b) The LSPR is associated with a large dipole moment, which can couple to the semiconductor, generating electron–hole pairs in the latter if occurring in a spectral region where the semiconductor absorbs light. This effect is referred to as plasmon-induced resonant energy transfer (PIRET).[36,37]

Subsequently, the plasmon resonance may dissipate either radiatively or nonradiatively. c) Radiative decay occurs via re-emission of photons (scattering) that may increase light absorption in the semiconductor if the plasmon energy is higher than the semiconductor bandgap. d) Nonradiative decay, also referred to as Landau damping, generates electron–hole pairs (with a nonthermal distribution) in the metal. Hot carriers rapidly relax to a thermal (Fermi–Dirac) distribution via electron–electron scattering, with a characteristic time of $\tau_{el} \approx 100$ fs–1 ps.[38–43] The resulting effective electron temperature equilibrates with the lattice by electron–phonon scattering in $\tau_{ph} \approx 1$–10 ps.[42,43] e) This process results in heating of the plasmonic material, which finally cools through heat transfer to the surrounding medium in 100 ps–10 ns, depending on the material, the particle size and the thermal conductivity of the environment.[16,44] In particular, heat generation is associated with Ohmic losses and is proportional to $\varepsilon''(\omega)|\boldsymbol{E}_{in}|^2$, where $\boldsymbol{E}_{in}$ is the electric field inside the material.[45] This heat can lead to a temperature rise of tens–hundreds of degrees depending on the incident power and the particular plasmonic excitation.[46,47] f) Alternatively, prior to their relaxation, hot charge carriers can be extracted from the plasmonic material and injected into the semiconductor: this process is referred to as hot electron (hole) injection and must occur within 1 ps from plasmon generation, in order to compete against electron–electron and electron–phonon scattering. This process is also referred to as indirect electron transfer, as recently a so-called direct electron injection process has been reported (g), where hot electrons (holes) are directly generated in the conduction (valence) band of an n-type (p-type) semiconductor in contact with the plasmonic material. This process occurs in 20–50 fs and is therefore

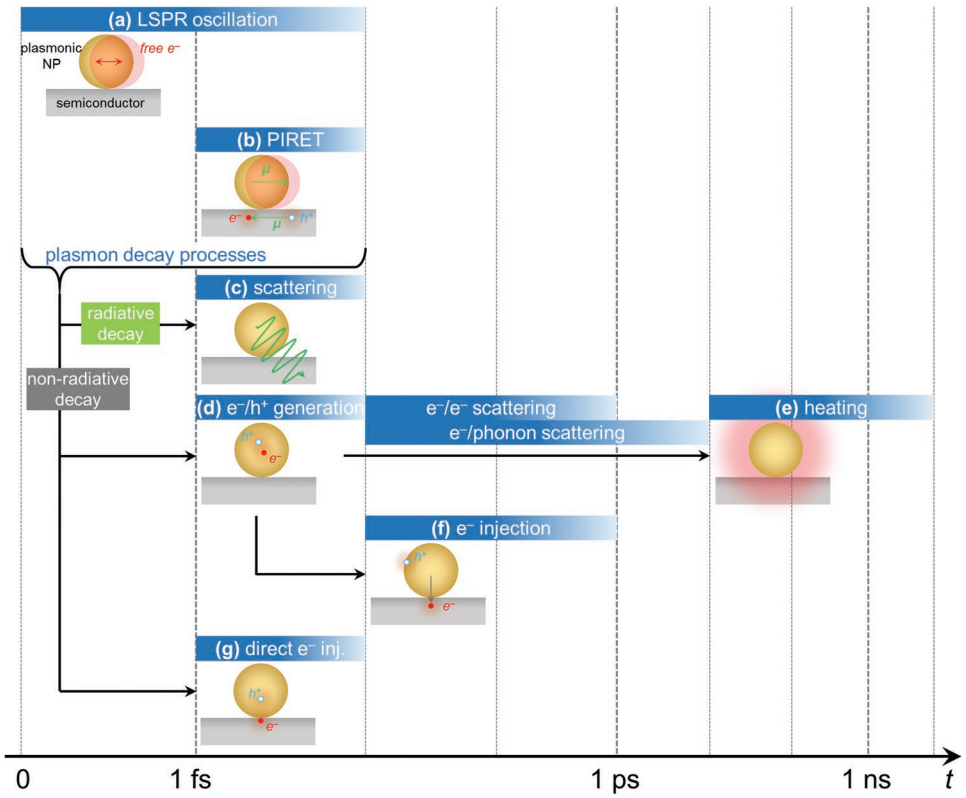

Figure 4. Schematic showing the time evolution of LSPR-excitation-induced processes occurring in a semiconductor/plasmonic nanostructure. a) LSPR oscillation. b) Plasmon-induced resonant energy transfer (PIRET). c) Scattering. d) Electron/hole generation. e) Plasmonic heating. f) Hot electron injection. g) Direct electron injection.

characterized by substantially faster dynamics than the indirect mechanism.[48–51] In both the direct and indirect processes, the interest in PEC water splitting resides in the possibility of generating additional charge carriers through the plasmonic unit, with energies lower than the bandgap.

The aforementioned mechanisms will be individually described in Section 3, and selected case studies from the literature will be presented.

2.2. Plasmonic Materials

The design of plasmonic photoelectrodes depends on the functionality that the material sustaining surface plasmons must provide and the physical location of plasmonic nanostructures, i.e., in the semiconductor, in the electrocatalyst or at several interfaces present in a PEC device.

Generally, traditional plasmonic materials include Au, Ag, Al, and Cu, and they have been widely investigated for various applications including PEC water splitting.[52–63]

Plasmonic materials for PEC water splitting must be low cost and exhibit chemical stability, corrosion resistance, high mechanical strength, high durability, and eventually good electrocatalytic activity.

Au and Ag are expensive, while Ag, Al, and Cu suffer from chemical instability as they are prone to oxidation. Although researchers have employed (for example) an alumina passivation layer for overcoming this instability, integrating such methods with a photoactive semiconductor growth can be challenging.[64,65] Noble metals often also suffer from low compatibility with complementary metal-oxide-semiconductor (CMOS) technology, which is paramount for PEC water splitting devices, since processing of the plasmonic material using the same fabrication methods as those employed for the semiconductor unit is preferred.

Owing to these limitations of traditional plasmonic metals, the last decade has witnessed a widespread search for alternative plasmonic materials.[66] Transition metal nitrides (TMNs) such as titanium nitride (TiN) and zirconium nitride (ZrN) have been proposed as suitable replacements for noble metals in plasmonics and PEC water splitting applications.[67–70] TMNs have very high thermal and chemical stability and can be processed with standard CMOS technologies.[71–75] More recently, transition metal dichalcogenides (MXenes) have received a remarkable attention for use in electrochemical energy-storage devices,[76–78] while their application in photonics and plasmonics is still developing.[79,80]

The most effective plasmonic material with suitable optical properties may be selected, based on the designed plasmonic enhancement mechanism of choice. The most direct strategy for evaluating candidate materials is to consider the real (ε') and the imaginary part (ε'') of the permittivity. From the former (ε') it is possible to retrieve the so-called crossover wavelength (λ where ε' becomes negative), which defines the spectral range where occurrence of the surface plasmon resonance is expected. It is an indication of the metallic nature of the material and a larger negative ε' usually provides larger absorption cross-section and enhancement of

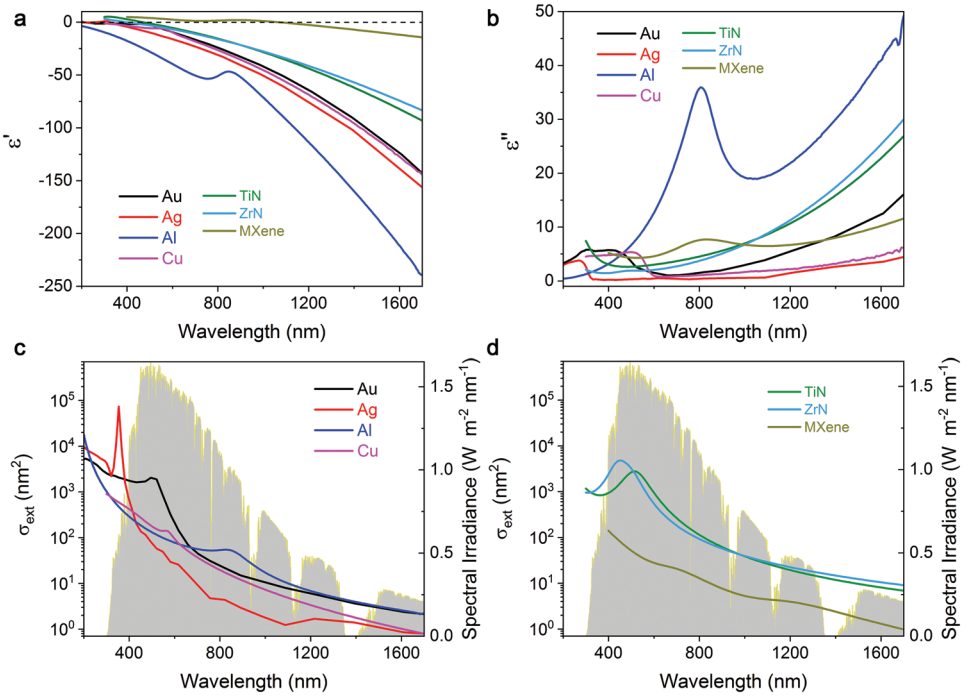

Figure 5. a,b) Optical properties of traditional plasmonic metals (Au, Ag, Al, and Cu) and alternative plasmonic materials (TiN, ZrN, and $Ti_3C_2T_x$ MXene, where T represents surface functional groups) showing the real part (ε') (a) and the imaginary part (ε'') (b) of the permittivity. Permittivity data taken from Johnson and Christy[82] for Au and Ag, McPeak et al.[83] for Al and Cu, Chaudhuri et al.[80] for MXene, and measured with variable-angle spectroscopic ellipsometry for TiN and ZrN. c,d) Extinction cross-sections (calculated by Mie theory for a 50 nm diameter spherical NP in air) for Au, Ag, Al, and Cu (c) and TiN, ZrN, and MXene (d) compared to the solar energy spectrum (ASTM G173-03 AM 1.5 Global).

the electromagnetic near field. In contrast, ε'' is a measure of the optical losses and a higher ε'' translates in a weaker surface plasmon resonance and a more dissipative decay to generate heat.

Figure 5a,b shows a comparison of ε' and ε'' for Au, Ag, Al, and Cu as well as for TiN, ZrN, and titanium carbide MXene. Ag shows the best compromise between high negative values of ε' and very low losses over the entire spectral range of all plasmonic materials. Au and Cu have the second-best optical properties with a high negative value of ε' and relatively low ε'', despite exhibiting higher losses (due to interband transitions) than Ag in the range 300–600 nm. Al is the most metallic material, having a cross-over wavelength at ≈100 nm, while simultaneously exhibiting the highest optical losses especially at ≈800 nm, where intense interband transitions strongly damp its metallic properties.[63,81]

On the other hand, the optical permittivity of TiN and ZrN (Figure 5a,b) epitaxial films highlights the excellent metallic behavior (large negative ε') and relatively low losses (small ε''), comparable to Au and Cu, of these materials in the visible and near-IR. In contrast, titanium carbide MXene is less metallic than TMNs and experiences a considerably lower loss (Figure 5a,b), which makes it ideally suited for plasmonics in the near-IR.[80]

To discuss the plasmonic efficiency of the different plasmonic materials, we compute the extinction cross-section (σ_{ext}) of a 50 nm diameter spherical particle made of Au, Ag, Al, Cu (Figure 5c) and of TiN, ZrN, and TiC MXene (Figure 5d). Al shows the highest σ_{ext} corresponding to the LSPR, but in the deep UV. Ag has a high σ_{ext}, comparable to that of Al, whereas Au and Cu exhibit a weaker σ_{ext} peak in the visible region. The nitrides show a σ_{ext} comparable to that of Au, peaking in the region 400–600 nm, while MXene shows a considerably weaker extinction peak.

Other plasmonic materials may be used in PEC water splitting, but have yet to be integrated in PEC devices. These include alkali metals (e.g., Na, Mg),[84–86] metal chalcogenides (e.g., $Cu_{2-x}S$, $Cu_{2-x}Se$, and $Cu_{2-x}Te$),[87] and transparent conductive oxides (TCOs), such as Al-doped ZnO (AZO), Ga-doped ZnO (GZO), and In-doped SnO_2 (ITO).[88,89]

3. Plasmon-Enhanced Water Splitting

In this section, we summarize all approaches that have made use of plasmonic resonances to boost the PEC water splitting by using optical effects. Here, we describe the different phenomena in plasmonic photoelectrodes by following the temporal evolution of surface plasmons after light excitation. Therefore, we consider examples focused on resonant energy transfer, scattering, hot electron injection, and thermal effects in PEC devices. Approaches employing SPPs (guided modes) and various photonic effects for enhanced PEC performance of the investigated semiconductor materials are discussed in a dedicated final paragraph.

3.1. Plasmon-Induced Resonant Energy Transfer

PIRET is a nonradiative energy-transfer mechanism occurring between plasmonic NPs and a nearby semiconductor prior to dissipation. PIRET is a variant of Förster resonant energy transfer (FRET),[90,91] which consists of a nonradiative downward energy transfer from a donor to an acceptor through dipole–dipole coupling. This mechanism depends on the overlap of the emission and absorption spectra of the two materials, the distance between them (usually few nm for FRET), as well as from the orientation of the respective dipole moments.

A clear distinction between PIRET and FRET, together with a rigorous mathematical treatment, has been reported by Wu and co-workers by using Au@SiO_2@Cu_2O (core@shell1@shell2, **Figure 6**a) NPs for the photocatalytic degradation of methyl orange dye and transient absorption spectroscopy

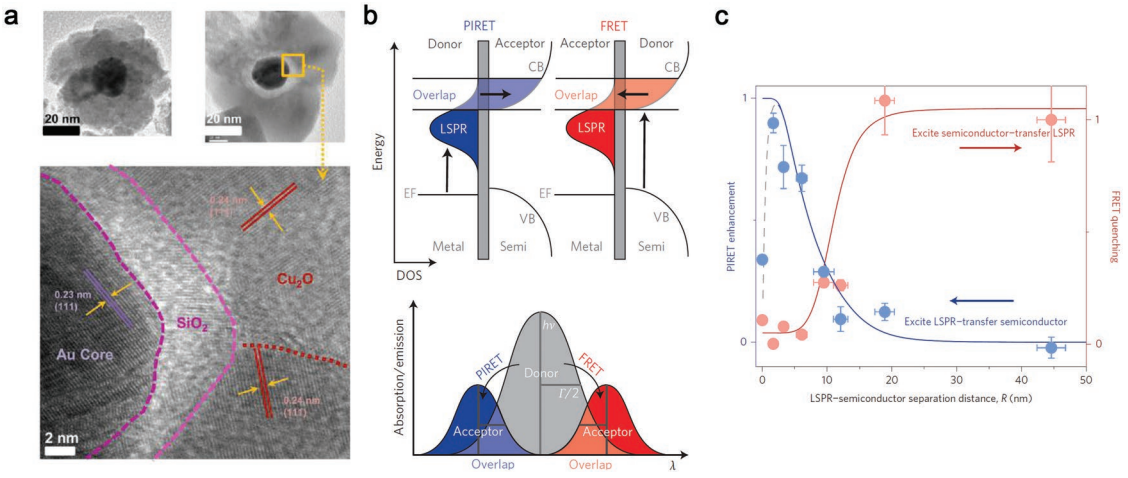

Figure 6. a) Transmission electron microscopy images of Au@Cu_2O (upper left) and Au@SiO_2@Cu_2O (upper right and bottom) NPs. b) Schematic of PIRET and FRET for a plasmon–semiconductor coupled dipole. c) Distance dependence of PIRET enhancement and FRET quenching for Au@SiO_2@Cu_2O NPs with different SiO_2 thickness. a) Reproduced with permission.[36] Copyright 2012, American Chemical Society. b,c) Reproduced with permission.[37] Copyright 2015, Nature Publishing Group.

experiments.[36,37] While FRET is an incoherent process, PIRET can be coherent. Since thermal relaxation of excited carriers can be much faster than spontaneous emission, a Stokes shifted energy transfer from the donor to the acceptor always occurs in FRET. In contrast, since plasmons dissipate via electron–electron interactions, plasmonic dipole (μ_{LSPR})–dipole (μ_{semi}) coupling can precede the Stokes shift, allowing either blue- or redshifted energy transfer. Figure 6b illustrates the energy transfer (top) and the spectral overlap (bottom) between the plasmon and the semiconductor. In PIRET, the plasmon is the donor and an excitation above the semiconductor bandgap can resonantly couple to the semiconductor and create electron–hole pairs. In FRET, the semiconductor is the donor and the excited state can be quenched by coupling to the redshifted plasmon resonance (Figure 6b). For unequal decay times, one dipole will build up population over the other and will store more energy on the average. When the lifetime of the plasmon is greater than that of the semiconductor dipole, then the population can be efficiently transferred to the semiconductor (PIRET). Conversely, FRET is observed in the opposite scenario.

Considering the similarity of FRET and PIRET, the metal–semiconductor interactions may be approximated as a dipole–dipole interaction and the corresponding energy transfer potential is given by

$$V_{\mathrm{DA}} = \frac{\kappa}{4\pi\varepsilon_0}\frac{\mu_{\mathrm{D}}\mu_{\mathrm{A}}}{R^3} \tag{13}$$

where μ_{D} and μ_{A} are the donor and the acceptor dipole moments, respectively, separated by a distance R and κ is an orientation factor.[92] The PIRET rate can be calculated by starting with the transition probability predicted by the FRET theory

$$w_{\mathrm{DA}} = \frac{9\kappa^2 c^4}{8\pi\tau_{\mathrm{D}^*}R^6}\int F_{\mathrm{D}}(\omega)\sigma_{\mathrm{A}}(\omega)\frac{d\omega}{n(\omega)^4\omega^4} \tag{14}$$

where τ_{D^*} is the donor lifetime, $F_{\mathrm{D}}(\omega)$ is the normalized donor fluorescence, $\sigma_{\mathrm{A}}(\omega)$ is the acceptor absorption coefficient, n is the refractive index, and c is the free-space speed of light;[36] F_{D} and σ_{A} are given as

$$F_{\mathrm{D}}(\omega) = \frac{\omega^3\tau_{\mathrm{D}^*}}{3\varepsilon_0\pi c^3}\left|\left\langle\psi_{\mathrm{D}^*}\left|\mu_{\mathrm{D}}\right|\psi_{\mathrm{D}}\right\rangle\right|^2\delta(E_{\mathrm{D}^*}-E_{\mathrm{D}}-\hbar\omega) \tag{15}$$

$$\sigma_{\mathrm{A}}(\omega) = \frac{\pi\omega}{3\varepsilon_0 c}\left|\left\langle\psi_{\mathrm{A}^*}\left|\mu_{\mathrm{A}}\right|\psi_{\mathrm{A}}\right\rangle\right|^2\delta(E_{\mathrm{A}^*}-E_{\mathrm{A}}-\hbar\omega) \tag{16}$$

where ψ_{D^*} (ψ_{A^*}) and ψ_{D} (ψ_{A}) correspond to excited and ground state wavefunctions having energy E_{D^*} (E_{A^*}) and E_{D} (E_{A}), respectively.

FRET efficiency (E) may be theoretically evaluated from the equation

$$E = \frac{w_{\mathrm{DA}}}{w_{\mathrm{DA}}+\sum w_{\mathrm{other}}} = \frac{1}{1+\left(\frac{R}{R_0}\right)^6} \tag{17}$$

where w_{other} is the sum of competing transfer processes (not considered in this case), and R_0 is the distance at which 50% of the energy is transferred.[37] R_0 is given by

$$(R_0)^6 = \frac{9\kappa^2 c^4}{8\pi}\int F_{\mathrm{D}}(\omega)\sigma_{\mathrm{A}}(\omega)\frac{d\omega}{n(\omega)^4\omega^4} = \tau_{\mathrm{D}^*}R^6 w_{\mathrm{DA}} \tag{18}$$

For PIRET, the relative enhancement of carrier creation in the semiconductor reads as

$$E = \frac{\alpha_{\mathrm{semi}}(\omega)+\alpha_{\mathrm{LSPR}}(\omega)\left[\frac{1}{1+\left(\frac{R}{R_0}\right)^6}\right]}{\alpha_{\mathrm{semi}}(\omega)} \tag{19}$$

where $\alpha_{\mathrm{semi}}(\omega)$ and $\alpha_{\mathrm{LSPR}}(\omega)$ are the absorption coefficients of the semiconductor and of the LSPR, respectively.

Li et al. demonstrated the FRET and PIRET dependence on distance between the plasmonic metal (Au) and the semiconductor (Cu_2O) through transient absorption spectroscopy with increasing SiO_2 spacer thickness.[37] FRET quenching of the Cu_2O fluorescence lifetime by the LSPR was measured at 500 nm for a 375 nm excitation and reads as

$$\mathrm{FRET}_{\mathrm{quenching}} = 1-E = 1-\left[1-\frac{\tau_{\mathrm{plasmon+semi}}}{\tau_{\mathrm{semi}}}\right] = \frac{\tau_{\mathrm{plasmon+semi}}}{\tau_{\mathrm{semi}}} \tag{20}$$

where E is described by Equation (17) and τ is the lifetime of the semiconductor (semi) or plasmon/semiconductor (plasmon+semi) system.

PIRET enhancement was determined, instead, by measuring the number of LSPR-excited carriers in the semiconductor by transient transmission at 10 ps after excitation, and calculated by

$$\Delta N = -\frac{1}{\sigma d}\ln\left(1+\frac{\Delta T}{T}\right) \tag{21}$$

where σ is the absorption cross section for the probe, d is the sample thickness, and $\Delta T/T$ is the transient signal.

The final results of these measurements are reported in Figure 6c, where the dependence of the semiconductor PIRET enhancement and FRET quenching on the gap between the plasmonic and the semiconductor NPs is considered. The distance dependence of these two energy-transfer processes in $Au@SiO_2@Cu_2O$ corresponds closely to the developed theory based on molecular FRET, and demonstrated that plasmon-semiconductor dipole–dipole coupling may be sustained over distances ≈20 nm or even longer, depending on the strength of the designed plasmonic resonance.

Several studies have considered the PIRET effect in PEC water splitting experiments.[93–100] In 2011, Ingram and Linic compared the performance of nitrogen-doped TiO_2 (N-TiO_2) decorated with Ag nanocubes (120 nm side, Ag/N-TiO_2) and Au NPs (25 nm diameter, Au/N-TiO_2).[93] N-TiO_2 exhibited an absorption onset at 500 nm, thereby preventing spectral overlap with Au NPs (λ_{LSPR} = 580 nm). This overlap was, however, possible with Ag (λ_{LSPR} = 410 nm). Therefore, the increase

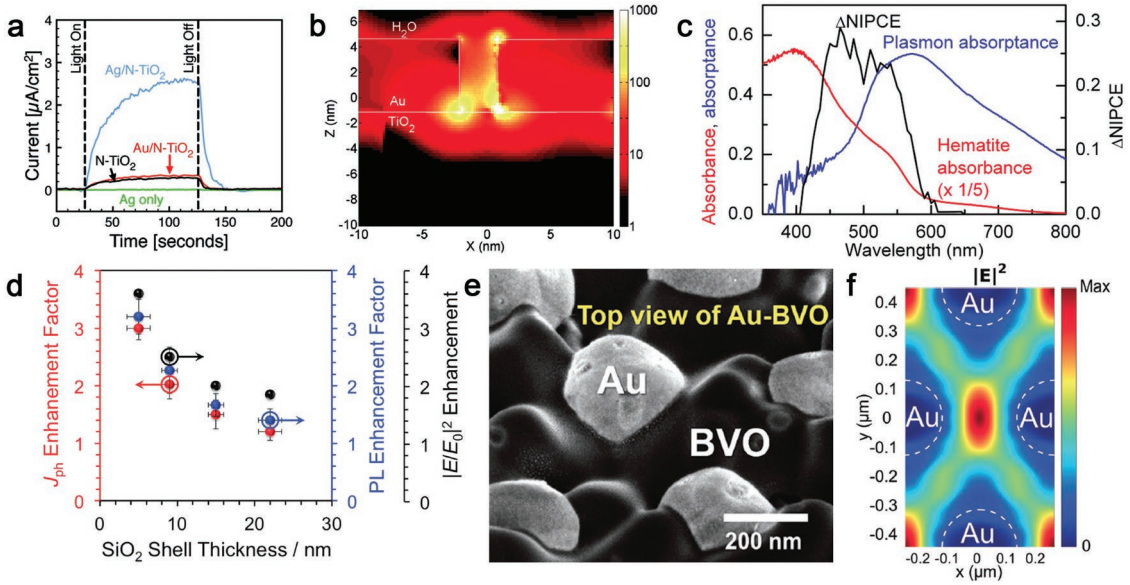

Figure 7. a) Photocurrent response for Ag (green), N-TiO_2 (black), Au/N-TiO_2 (red), and Ag/N-TiO_2 (light blue) upon illumination with $400 < \lambda < 900$ nm. Reproduced with permission.[93] Copyright 2011, American Chemical Society. b) Electric field intensity at the Au/TiO_2 interface calculated using FDTD methods starting from a top-view SEM image. Reproduced with permission.[94] Copyright 2011, American Chemical Society. c) Difference between the normalized IPCE of α-Fe_2O_3 with and without Au NPs (ΔNIPCE, black) compared to the LSPR (blue) and α-Fe_2O_3 (red) optical spectra. Reproduced with permission.[95] Copyright 2011, American Chemical Society. d) Photocurrent (J_{ph}, red), photoluminescence (PL, blue), and electromagnetic field ($|E/E_0|^2$, black) enhancement factors for the plasmonic Cu_2O/Au@SiO_2 photocathodes with different SiO_2 shell thicknesses. Reproduced with permission.[97] Copyright 2016, Wiley-VCH. e) Top-view SEM of ordered Au nanosphere patterned array embedded in a Mo:$BiVO_4$ photoanode and f) corresponding simulated $|E|^2$ field distribution at 500 nm. e,f) Reproduced with permission.[98] Copyright 2017, Wiley-VCH.

in the photocurrent with broadband visible illumination of Ag/N-TiO_2 (**Figure 7**a) was attributed to PIRET. Conversely, Liu et al. reported the occurrence of this mechanism for the case of Au/TiO_2, where significant enhancements (by factors of 5 and 66) in photocurrents were measured with 523 and 633 nm illumination wavelengths, respectively.[94] These results were explained by considering electric field hot spots between Au nanoislands on top of TiO_2 (Figure 7b) and nonzero visible light absorption of the semiconductor due to defects formed during the synthesis process.

Thimsen et al. modified α-Fe_2O_3 platelets with Au NPs in surface configuration.[95] These modified platelets generated a lower photocurrent with respect to pristine hematite; however, owing to the PIRET effect, the normalized incident photon-to-current efficiency (IPCE) of the composite photoanodes increased in the superposition region between the semiconductor absorption and the LSPR resonance (Figure 7c). A similar system composed of α-Fe_2O_3 planar film and Au NPs was reported by Thomann et al.[100] In this work, the photocurrent generated at wavelengths corresponding to the band edge of α-Fe_2O_3 doubled when Au NPs were either completely or partially embedded in the semiconductor film. The varying location of plasmonic NPs allowed to control the spectral range width of both absorption and photocurrent enhancement due to constructive or destructive interference of light propagating into the α-Fe_2O_3 films.

DuChene et al. have recently investigated the PIRET mechanism in plasmonic photocathodes assembled by decorating a Cu_2O nanowire network with Au@SiO_2 (core@shell) NPs.[97] The photocurrent tripled (10–30 μA cm^{-2}) when the pristine Cu_2O was functionalized with Au@SiO_2 NPs. A corresponding IPCE enhancement was observed in the 450–600 nm spectral range, perfectly matching the overlap in absorption between Au@SiO_2 NPs and Cu_2O nanowires. The occurrence of PIRET was verified by testing photocathodes including plasmonic Au@SiO_2 NPs having different thickness of SiO_2 shell (5, 9, 15, and 22 nm). The highest photocurrent enhancement was observed for the thinnest SiO_2 shell (Figure 7d), while an exponential decay occurred for the other samples, closely resembling the results reported by Li et al.[37] The same trend was also found both for the photoluminescence and the simulated electric field enhancement factor, confirming that the PIRET was responsible for the enhancement performance.

Finally, Kim et al. reported a Mo:$BiVO_4$ photoanode interwoven in a hexagonal pattern of Au NPs (Figure 7e).[98] The Au/Mo:$BiVO_4$ photoanode showed a current density of 2.83 mA cm^{-2} at 1.23 V vs RHE, 2.2 times higher than that of the bare Mo:$BiVO_4$ photoanode. The external quantum efficiency (EQE) increased considerably up to 500 nm, and a significant integrated enhancement of a few percent occurred in the range of 500–700 nm. The authors verified a strong absorption enhancement in the Au/Mo:$BiVO_4$ photoanodes with respect to the bare Mo:$BiVO_4$ films in specific locations corresponding to electromagnetic hot spots (Figure 7f). The occurrence of PIRET was determined by low-temperature time-correlated single photon counting and transient absorption. These results clearly showed an increased lifetime of photogenerated charges in Au/Mo:$BiVO_4$ than in pristine Mo:$BiVO_4$. The reduced charge recombination indicated that PIRET dominated over the hot electron injection mechanism in Au/Mo:$BiVO_4$ photoanodes.

3.2. Scattering

Figure 8a shows a schematic of the scattering effect, originating from the radiative decay of a LSPR. Symmetrical photon emission occurs when the plasmonic NPs are embedded in a homogeneous medium, while it is preferentially directed toward the material with the highest refractive index n for NPs close to an interface between different media.[101] This holds for aqueous electrolytes ($n \approx 1.3$) in contact with typical semiconductors used for water splitting ($n \approx 2.6$ for TiO_2 and $n \approx 2.9$ for α-Fe_2O_3); thus, a sort of antireflection layer can be obtained by placing plasmonic NPs at the electrolyte/semiconductor interface. Moreover, in the case of several closely spaced NPs, multiple scattering events can occur, leading to a substantial increase in the light pathway within the semiconductor, similar to that reported for solar cells.[102]

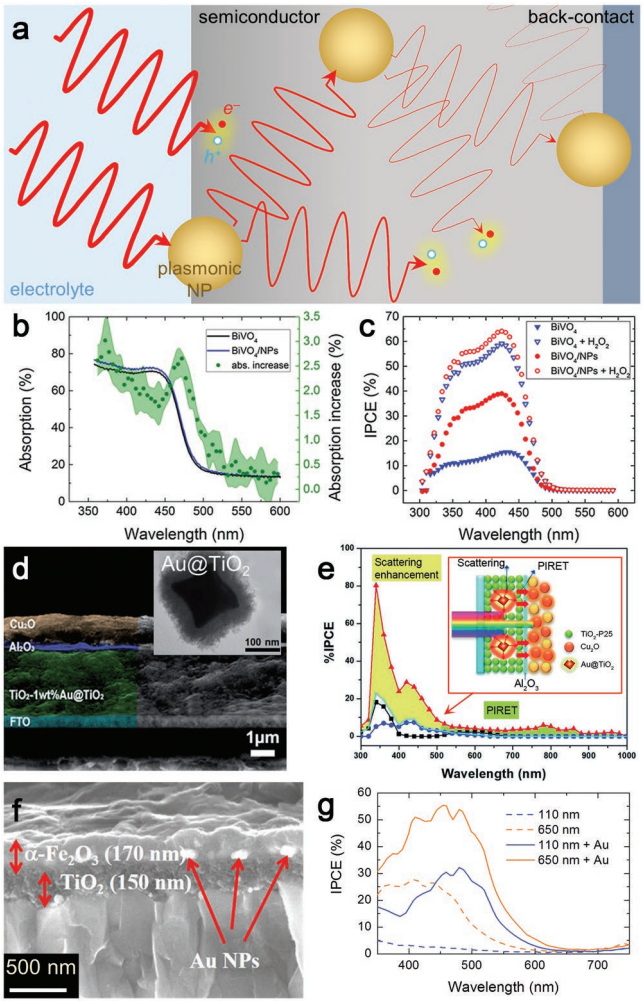

Figure 8. a) Schematic of the plasmonic scattering effect in semiconductor photoelectrodes. b) Absorption increase in $BiVO_4$ decorated with 65 nm Au NPs in back-illumination configuration. c) IPCE measurements of $BiVO_4$ photoanodes before and after decoration with Au NPs and with/without H_2O_2 as a hole scavenger in the electrolyte solution. d) SEM image of TiO_2–Au@TiO_2/Al_2O_3/Cu_2O photoelectrode on FTO substrate (inset: TEM image of an individual Au@TiO_2 unit). e) IPCE spectrum of the composite photoelectrode in d) (red triangles) compared with the spectra of TiO_2–Au@TiO_2 (black squares), Cu_2O (blue circles), and TiO_2/Cu_2O (light-blue line). The inset shows schematics of the proposed enhancement mechanism. f) SEM image of α-Fe_2O_3 photoanode with Au NPs at the interface with a TiO_2 layer underneath. g) IPCE spectra of α-Fe_2O_3 photoanodes (thicknesses: 110 and 650 nm) with or without Au NPs. b,c) Reproduced with permission.[103] Copyright 2016, Wiley-VCH. d,e) Reproduced with permission.[106] Copyright 2015, Royal Society of Chemistry. f,g) Reproduced with permission.[107] Copyright 2015, American Chemical Society.

Valenti et al. reported a scattering effect for 65 nm Ag NPs on top of 100 nm-thick $BiVO_4$ photoanodes.[103] At energies higher than the bandgap, the absorption of the composite material was moderately higher than that of bare $BiVO_4$ (Figure 8b), thus evidencing a radiative plasmon decay by scattering. The IPCE spectra of the pristine and Ag-NP-decorated films were measured with a hole scavenger (i.e., H_2O_2) with back-illumination (Figure 8c). This analysis revealed that in H_2O_2 the NPs yielded a relatively small increase in the photoactivity, which was attributed to scattering effects. The larger IPCE enhancement in the absence of the hole scavenger, conversely, was related to catalytic effects of Ag NPs[104] (see Section 4). A higher IPCE increase (≈6%) could be obtained by front illumination.

Zhang et al. also combined Au NPs with $BiVO_4$ and studied the size-dependent plasmonic effects through PEC characterizations and finite-difference time-domain (FDTD) simulations.[105] In particular, the scattering effect was predominant for Au NPs larger than 60 nm, while FDTD simulations suggested that PIRET occurred for smaller NPs (≤40 nm). Scattering and PIRET were also reported for a heterojunction photoelectrode composed of p-type Cu_2O and n-type TiO_2 that was loaded with 1 wt.% Au@TiO_2 core-shell NPs with different Au-core sizes (37–120 nm).[106] Figure 8d shows a scanning electron microscopy (SEM) image of the device, which also included an insulating Al_2O_3 layer between TiO_2 and Cu_2O for improved interfacial charge separation. The cathodic photocurrent generated by the photoelectrodes increased gradually with increasing Au particle size, reaching a maximum value of –4.34 mA cm^{-2}, which is almost 20 times higher than that of the TiO_2/Cu_2O photoelectrode. IPCE measurements confirmed that the maximum performance was achieved with 120 nm NPs (Figure 8e). This enhancement was attributed to scattering (in the UV range) as well as PIRET effects (visible–NIR range) depending on the incident wavelength. Archana et al. reported scattering and catalytic effects from Au NPs (≈80 nm diameter) embedded at the α-Fe_2O_3/TiO_2 layer interface of composite photoanodes (Figure 8f).[107] The LSPR of Au NPs occurred at ≈600–700 nm and the IPCE of films with different α-Fe_2O_3 thicknesses (110 and 650 nm) increased at wavelengths below 600 nm, i.e., in the spectral region of the semiconductor absorption (Figure 8g). In particular, the inclusion of Au NPs led to a stronger enhancement for the thinner film. This was ascribed to a stronger scattering effect as, compared with the thicker film, the Au NPs could better interact with light.

3.3. Hot Electron Injection

Hot electron injection may be either direct or indirect and is one of the most widely investigated plasmonic mechanisms for enhancing the efficiency of PEC water splitting. This mechanism enables the use of visible and NIR photons that are not

absorbed by wide-bandgap semiconductors typically employed as photoelectrodes.

3.3.1. Indirect Mechanism

When a Schottky barrier is formed at a metal/semiconductor interface (**Figure 9**a), the barrier height (Φ_{SB}) can be roughly evaluated with the Schottky–Mott rule[108,109]

$$\Phi_{SB} = \varphi_m - \chi_s \tag{22}$$

where φ_m is the metal work function and χ_s is the semiconductor electron affinity. This simple rule neglects other parameters, such as structural/electronic inhomogeneity, quantum tunneling and interfacial chemical effects, that may lower Φ_{SB}.[110–112]

The indirect mechanism (Figure 9a) consists of three elementary steps: i) hot electron generation upon plasmon decay, ii) electron transport to the interface with the semiconductor, and iii) the transfer of those with energy higher than Φ_{SB} to the semiconductor CB.[113,114]

Hot electron injection is not peculiar of plasmonics, but it is the working mechanism of Schottky diodes.[115] The photocurrent in the diode can be expressed in terms of Fowler's law as[116]

$$I = c\frac{(h\nu - \Phi_{SB})^2}{h\nu} \tag{23}$$

where c is a constant and $h\nu$ is the photon energy. The value of Φ_{SB} can be determined by fitting the experimental photocurrent with Equation (23), and compare it with that determined from Equation (22). In the case of plasmonic metals in contact with semiconductors, a deviation from Fowler's law is introduced by the plasmon resonance, as shown in Figure 9b for an Au/TiO_2 diode.[117] This law can then be modified in order to determine the photocurrent in the plasmonic diode (I_{plasm}):[113]

$$I_{plasm} = I \cdot A \tag{24}$$

where A is the plasmon absorption spectrum. This is illustrated in Figure 9c for Au/Si diodes in which Au has the form of nanorods.[113]

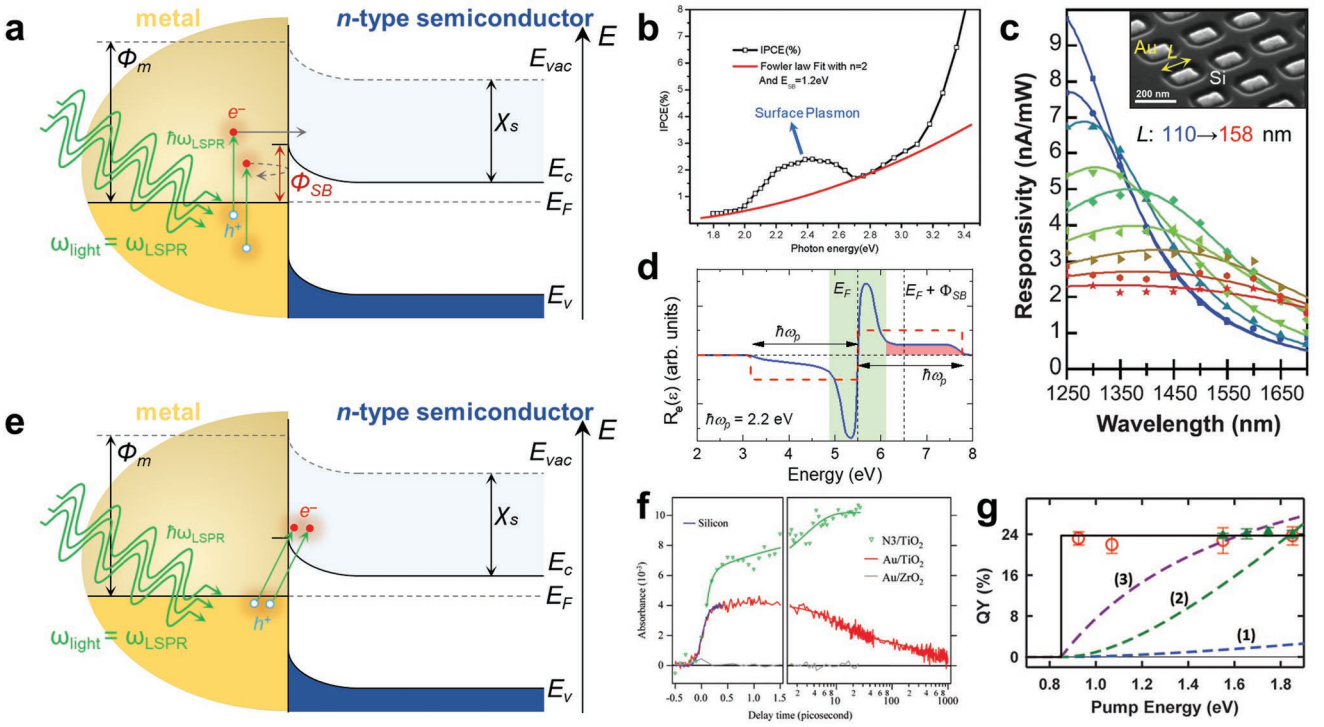

Figure 9. a) Schematics of indirect hot electron injection from a plasmonic metal to an n-type semiconductor (E_{vac}: vacuum energy; E_F: Fermi level; ϕ_m: work function of the metal; χ_s: electron affinity of the semiconductor; Φ_{SB}: Schottky barrier). b) IPCE of a plasmonic Au/TiO_2 diode. b) Reproduced with permission.[117] Copyright 2011, American Chemical Society. c) Experimental photocurrent of Au nanoantennas/Si diodes for different antenna lengths (points); solid lines represent the fit of Equation (24) to the data for Φ_{SB} = 0.5 eV. Reproduced with permission.[113] Copyright 2011, American Association for the Advancement of Science. d) Solid line: typical spectrum showing the rate of electron generation in a localized plasmon wave in a metal nanocube; two types of excited intraband carriers can be observed: Drude (green region) and hot carriers (red region). Dashed line: approximated "box-like" distribution of generated electrons. Reproduced with permission.[118] Copyright 2017, American Chemical Society. e) Schematic of direct hot electron injection from a plasmonic metal to an n-type semiconductor. f) Transient absorption kinetics at 3500 nm of nanocrystalline films (green: N3/TiO_2; red: Au/TiO_2; gray: Au/ZrO_2). The blue line shows the response of the apparatus obtained using a Si plate. f) Reproduced with permission.[48] Copyright 2007, American Chemical Society. g) Measured quantum yield of direct electron injection in quantum dots (red open circles: PbS; green triangles: Cd_3P_2) and yield predicted from three different variations of Fowler's equation (dashed lines). Reproduced with permission.[51] Copyright 2015, American Association for the Advancement of Science.

The generation of hot carriers has been theoretically modeled by several groups using different degrees of approximation, as discussed in detail elsewhere.[118–125]

For example, Govorov and co-workers formulated a quantum theory for plasmonic hot carriers generation and injection under optical excitation.[118–120] Figure 9d shows an example of a nonequilibrium distribution of charge carriers in a localized plasmon wave in a metal nanostructure.[118] Most electrons and holes are generated with an energy close to the Fermi level (Drude carriers), while higher energy charge carriers (hot) are also present and are formed by quantum optical transitions near the surfaces, which in turn can occur due to the breaking of linear momentum conservation. The ratio between the generation rates of hot and Drude carriers is proportional to $1/d^2$, where d is the NP diameter.[126] Thus, the likelihood of hot electron injection into a semiconductor increases with decreasing size of the NP. The generation rate of high-energy electrons capable of crossing the Schottky barrier reads as[111]

$$\mathrm{Rate}_{\mathrm{high}-E} = \frac{2}{\pi^2}\frac{e^2E_\mathrm{F}^2}{\hbar}\frac{\hbar\omega-\Phi_\mathrm{SB}}{(\hbar\omega)^4}\int_\mathrm{S}\left|E_\mathrm{norm}\left(\vartheta,\varphi\right)\right|^2\mathrm{d}s \tag{25}$$

where E_F is the Fermi level of the metal and $E_\mathrm{norm}(\vartheta,\phi)$ is the normal component of the internal electric field near the NP surface.

On the other hand, Atwater and co-workers reported a nonsymmetrical energy distribution of hot carriers for Au and Cu, where, compared to hot electrons, a higher fraction of hot holes was located farther from E_F.[121,122] Dal Forno et al.[125] have indeed recently demontrated that Au is particularly suitable for generating hot holes for the OER. While it is possible to calculate the energy distribution of the generated hot electrons, it is less known the distribution of the injected ones in the semiconductor. A recent article by Cushing et al.,[127] in this regard, showed that a "box-like" energy distribution (see dashed line in Figure 9d) was sufficient to estimate the energy of injected carriers in Au@TiO_2 core–shell nanostructures, which was actually higher than the bottom of the CB. In other words, nonthermal electrons were injected, which may lead to a higher thermodynamic driving force for the water splitting process.

3.3.2. Direct Mechanism

Figure 9e shows a schematic of the direct hot electron injection for a metal/n-type semiconductor. In contrast to the indirect mechanism, the LSPR decays providing the direct generation of hot electrons in the semiconductor CB and of hot holes in the metal, respectively, without any intermediate step.

The direct mechanism has been theoretically proposed by Long and Prezhdo[50] for a Au_{20} cluster on TiO_2, where a considerable delocalization of the plasmon on TiO_2 and a high probability (50%) of direct electron localization in the TiO_2 CB occur 40 fs after optical excitation. The aim of the model was to find a theoretical basis for the experimental results reported by Furube et al.,[48] who observed that an electron transfer in Au/TiO_2 occurred in ≤240 fs (Figure 9f). A follow-up study on Au/TiO_2 found that the electron injection was complete in 50 fs, with an efficiency of 20–50%, depending on the TiO_2 particle size.[49]

However, in 2015 Wu et al. investigated colloidal CdSe nanorods functionalized with Au NPs and reported the first clear experimental evidence pointing to the existence of the direct pathway.[51] They found that an ultrafast electron transfer from Au to CdSe occurred within 20 ± 10 fs and obtained a quantum yield of 24% independent of the pump energy (Figure 9g). However, theoretical curves calculated from Fowler's equation are inconsistent with experimental data (see the figure): as plasmon decay directly excited an electron from Au to CdSe, the quantum yield was independent of the excess energy of the electron above the CB edge. In 2017, Tan et al. measured a hot electron transfer from Ag NPs (4 nm diameter) on TiO_2 occurring in ≤10 fs.[128] The direct mechanism has recently been identified, but a systematic study on indirect versus direct pathways in PEC water splitting experiments has yet to be performed.

3.3.3. Nanostructure and Material Design Strategies

The prototypical material combination is TiO_2/Au,[129–131] owing to the fact that TiO_2 can fully take advantage of hot electron injection due to its wide bandgap of 3.0–3.2 eV.

In general, one typical feature of wide-bandgap semiconductors decorated with plasmonic metal NPs is a change in optical spectra, as illustrated in **Figure 10**a for ZnO nanorods covered with Au NPs.[132] However, optical measurements are not sufficient to discern the plasmonic mechanism in action. Hot electron injection must be experimentally verified by wavelength-dependent photocurrent measurements, assessing at the same time a photoresponse at wavelengths beyond the semiconductor absorption threshold and a superposition between the photocurrent spectra and the plasmon resonance. Figure 10b shows typical photocurrent curves for Au/ZnO nanostructured photoanodes. The photocurrents generated under visible-light illumination ($\lambda > 420$ nm) correspond to the optical spectra of Figure 10a; as $E_\mathrm{g} = 3.37$ eV (≈368 nm) for ZnO,[133] the authors attributed the nonzero photocurrent to hot electron injection from Au NPs to the ZnO CB. Fitting of the experimental data with Fowler's law, yielded a comparable trend to the plasmonic absorption peak of Au NPs, thereby highlighting the role of hot electron injection in enhancing the PEC performance.[132]

A similar approach consists in measuring the IPCE spectrum of the composite system and finding a clear correspondence with the absorption one.[96,112,130,132,134–138] For example, Pu et al. synthesized TiO_2 nanowires decorated with Au NPs, nanorods (NRs) or both. The decorated nanowires, in contrast to bare TiO_2, exhibited a nonzero IPCE in the visible region, which was attributed to the hot electron injection mechanism (Figure 10c).[96]

Mi et al.[134] reported the strategy illustrated in Figure 10d: starting from an Al_2O_3 template, Al nanocone arrays were obtained, which were covered with AZO and TiO_2 by atomic layer deposition and, finally, with Au NPs by evaporation. The use of AZO increased the electron conductivity toward the Al metal contact and the counter-electrode. The Au NPs introduced a visible-light activity and increased UV-light activity through hot electron injection (yielding a photocurrent of

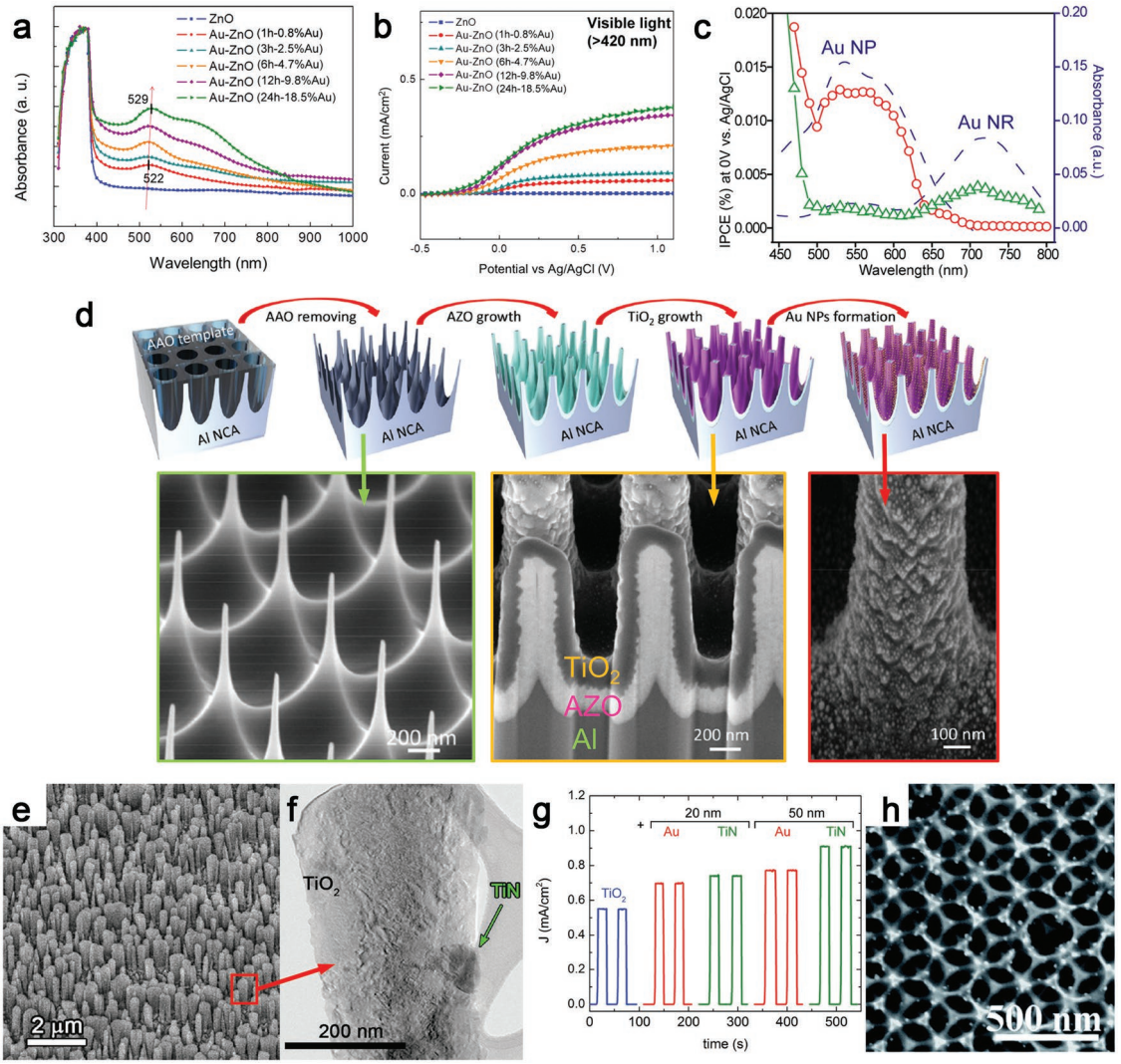

Figure 10. a) Absorption spectra and b) linear sweep voltammograms (in 0.5 M aqueous Na_2SO_4 solution, pH 6.8) of Au–ZnO photoanodes. Reproduced with permission.[132] Copyright 2012, American Chemical Society. c) IPCE spectra of TiO_2 nanowires decorated with Au NPs (≈8 nm diameter) and Au NRs (15 nm × 40 nm) compared with their corresponding absorption spectra. Reproduced with permission.[96] Copyright 2013, American Chemical Society. d) Schematic of the procedure for realizing AZO/TiO_2/Au nanocone arrays (top) and SEM images showing some steps of the synthesis process (bottom). Reproduced with permission.[134] Copyright 2015, Wiley-VCH. e) SEM image, f) TEM image, and g) chopped photocurrents at 1.23 V vs RHE under 150 mW solar irradiation of TiO_2 nanowires (grown with glancing angle deposition) decorated with TiN nanocubes, compared to photocurrents generated from the nanowires with Au NPs and the pristine TiO_2. e–g) Reproduced with permission.[111] Copyright 2017, Wiley-VCH. h) SEM image of Au-NP-decorated TiO_2 photonic crystals on NRs. Reproduced with permission.[136] Copyright 2014, Royal Society of Chemistry.

0.04 mA cm^{-2} under $\lambda \geq 455$ nm at 0.2 V vs RHE) and the PIRET effect, respectively.

Other authors have studied the effect of changing the plasmonic material used in combination with TiO_2 nanostructures. For example, TiO_2 nanowires were grown by glancing angle deposition (GLAD) and functionalized with either Au or TiN NPs with average diameters of 20 and 50 nm (Figure 10e,f).[111] Compared with Au, TiN offers a broader plasmon resonance at comparable wavelengths, higher thermal and mechanical stability, and forms an Ohmic junction with TiO_2, owing to its low work function (ϕ_{TiN} = 4 eV, ϕ_{Au} = 5.2 eV).[67,139] Accordingly, functionalization of TiO_2 nanowires with TiN yielded greater photocurrent enhancement than functionalization with Au NPs (Figure 10g). This was attributed to an increase in the efficiency of hot carrier collection from both interband transitions and plasmon decay.[111] Finally, photonic crystals have been considered in studies on hot electron-enhanced PEC water splitting.[136,137] In particular, Zhang et al.[136] reported a TiO_2 bilayer morphology consisting of a photonic crystal (pore diameters: 250 nm) on top of vertically oriented NRs (diameter: ≈100 nm, length: ≈2 μm). The photonic crystal was subsequently decorated with Au NPs (10 nm diameter), as shown in Figure 10h. The visible-light activity of this device was attributed to the synergistic combination of i) the so-called slow photon effect, i.e., the decrease of group velocity of photons having energies close to the photonic bandgap, and ii) the

LSPR of Au NPs, which occurred in the same spectral region, thus resulting in efficient hot electron injection and an IPCE of 6% at 550 nm.

3.4. Thermal Effects

The temperature increase in metal nanostructures upon plasmonic excitation, i.e., the so-called thermoplasmonic effect,[44,140] has been employed in many fields,[44,141] although it has only rarely been investigated from the viewpoint of PEC water splitting.

In 2002, Licht proposed that the water splitting efficiency could be increased through the application of high temperatures.[142] More recently, Pihosh et al. reported a high photocurrent of 18.2 mA cm^{-2} by $WO_3/BiVO_4$ NRs under the combined effect of heating and light concentration (3 Suns at 50 °C).[143] The specific effect of temperature was attributed to improved reaction kinetics at the photoelectrode/electrolyte interface, which counter-balanced the enhanced charge recombination in $BiVO_4$.

Chueh and co-workers have evaluated the temperature-dependent photocurrent of α-Fe_2O_3,[144] $BiVO_4$,[145] and reduced TiO_2[146] and found that the minority carrier diffusion length, L_D, increased with heating of the semiconductor material. **Figure 11**a shows that the diameter-dependent photocurrent generated by TiO_2 nanowires increased monotonically with increasing temperature (from 10 °C to 70 °C). Figure 11b shows the photocurrent produced by nanowires, modeled with the addition of a temperature-dependent L_D (with an Arrhenius behavior). L_D values of ≈5 and ≈9.5 nm occurred at 25 °C and 70 °C, i.e., the hole mobility increased significantly with temperature. Therefore, by employing thermoplasmonic nanostructures (rather than an external power supply) as heat sources, this approach has considerable potential for enhancing the PEC performance of earth-abundant transition metal oxides.

On the other hand, the thermal effects of plasmonic NPs have been investigated for their role in photocatalytic reactions related to water splitting. Agarwal et al.[147] have studied the heating induced by laser illumination (532 nm) of Si nanowires (diameter: 100 nm) coated with an Au film (10 nm). A peak temperature of ≈1000 K was achieved with TM polarization (intensity: 5.7×10^5 W cm^{-2}). Subsequently, a 5 nm thick coating of TiO_2 NRs was applied in order to assess these devices for H_2 production from the photoreforming of ethanol via the combined effects of light and heat (Figure 11c). Samples without the TiO_2 layer (Si/Au) and without the Si nanowires (Au/TiO_2) were also tested and compared with the "complete" architecture ($Si/Au/TiO_2$). While Si/Au was completely inactive, $Si/Au/TiO_2$ exhibited higher H_2 production than Au/TiO_2 films, owing to the heat generated within the Si nanowires (see Figure 11d).

In another study, Bora et al.[47] prepared Au-NP-decorated ZnO NRs (Figure 11e) and used a laser illumination (wavelength: 532 nm, intensity: 100 W m^{-2}) to obtain a localized heating (temperature of ≈90 °C). The methylene blue (MB) degradation in the decorated NRs was higher than that of bare ZnO NRs, owing to the combination of hot electron injection to the CB of ZnO and plasmonic heating, which increased the interaction between photogenerated charges and MB molecules. Furthermore, the activation energy E_a was estimated from Arrhenius plots (Figure 11f) by subjecting bare ZnO and Au–ZnO NRs to photocatalytic experiments at different temperatures. Owing to plasmonic heating and other plasmonic effects, E_a decreased with increasing temperature. Matranga and co-workers obtained similar results for two-step CO_2 reduction (reverse water-gas shift and CO methanation).[148]

In each of these studies, plasmonic-heating-induced changes in temperature were assessed by Raman spectroscopy.[47,147,148] Indeed, certain modes of semiconductor materials, such as Si,[149] ZnO,[150,151] and TiO_2,[152,153] exhibit a temperature-dependent broadening and/or shift, which allows contact-less and local temperature measurements after suitable calibration with controlled

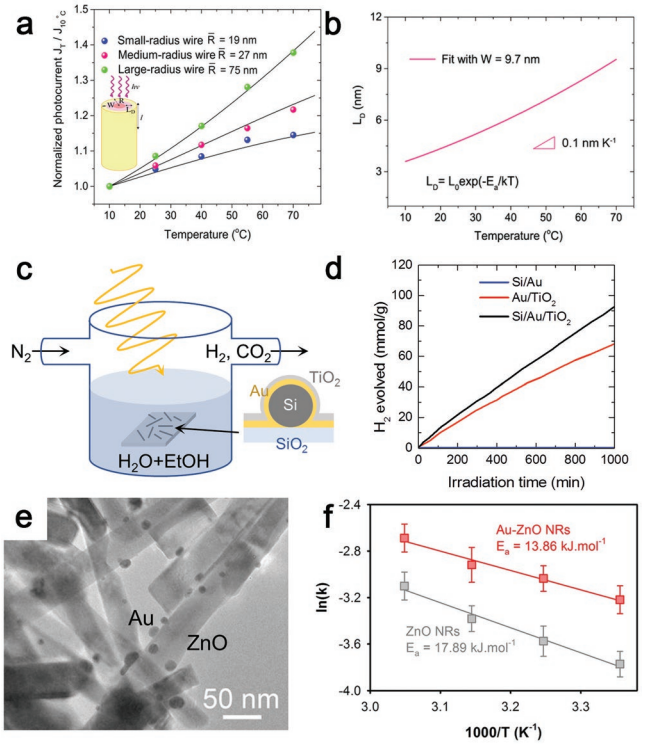

Figure 11. a) Comparison of the normalized photocurrent at 1.0 V vs RHE as a function of the temperature for TiO_{2-x} nanowires with different radii under 1 Sun illumination in 1 M NaOH/0.1 M Na_2SO_3. b) Temperature-dependent minority carrier diffusion length, L_D, calculated based on Arrhenius behavior, where L_0 and E_a are obtained from fitting the data in (a) with the space charge region width W_{sc} = 9.7 nm. c) Schematic of the photocatalysis setup for testing the Au-coated Si nanowire devices with TiO_2 NRs fabricated on a glass substrate ($Si/Au/TiO_2$). d) H_2 evolution volume during catalytic photoreforming of ethanol, using the three different devices, during irradiation with a 300 W Hg/Xe lamp. e) TEM image of Au–ZnO NRs (diameter of Au NPs: 7–23 nm). f) Arrhenius plot showing the activation energy E_a for the photocatalytic degradation of MB under solar light in the presence of bare ZnO and Au–ZnO NRs. a,b) Reproduced with permission.[146] Copyright 2017, American Chemical Society. c,d) Reproduced with permission.[147] Copyright 2017, American Chemical Society. e,f) Reproduced under the terms of the CC-BY Creative Commons Attribution 4.0 International License (http://creativecommons.org/licenses/by/4.0/).[47] Copyright 2016, Springer Nature.

heating.[154,155] On the other hand, thermal effects have also been probed through scanning electrochemical microscopy.[156]

3.5. Guided Modes and Other Photonic Effects

In this section, we provide an overview of examples that have made use of SPP or guided modes (see Section 2) and other photonic effects combined with LSPR to enhance the PEC water splitting performance. Photonic modes are usually observed when periodic nanostructured arrays present at least one dimension comparable to the incident wavelength, whereas plasmonic resonances occur for subwavelength nanostructures.[157]

Li et al. have reported a one order of magnitude increase in the photocurrent generated by α-Fe_2O_3 NRs grown inside an Au nanohole array (**Figure 12**a–e) supporting SPP modes having resonance wavelengths that could be efficiently absorbed as waveguided modes through above-bandgap transitions in α-Fe_2O_3.[158] The guided modes resulted in an IPCE enhancement of 20% at 400 nm, while the weak LSPR resonance at 600–700 nm, due to edges of Au nanohole array, contributed marginally (by ≈0.1%) to the photocurrent enhancement through hot electron injection.

Xu et al. have recently reported the fabrication of a large-area CdS/Au truncated pyramid array (PTP) as photoanodes obtained by using an anodic aluminum oxide template prepared by anodization (Figure 12f).[159] If a CdS/Au planar structure was taken as the reference, CdS/Au pillars and PTP yielded significant light absorption over the entire visible spectrum (Figure 12g). Accordingly, under 1 Sun illumination, the photocurrent of the PTP structure (1.6 mA cm^{-2}) was higher than that of the CdS/Au planar one (0.8 mA cm^{-2}). This enhancement was reflected in the IPCE spectra (Figure 12h), that revealed a significant contribution in the range 300 nm < λ < 480 nm, and a lower enhancement at longer wavelengths. FDTD simulations provided a fundamental understanding of the enhanced performance observed in CdS/Au PTP photoanodes. Figure 12i shows the simulated electric field distributions $|\boldsymbol{E}/\boldsymbol{E}_0|$ over one CdS/Au PTP at 350 nm, revealing that the strong enhancement in the photocurrent below 480 nm was due to photonic modes related to the periodic arrangement of PTP nanostructures. These modes resonated at wavelengths matching the CdS bandgap and enabled efficient absorption through scattering and PIRET. Otherwise, the photocurrent enhancement occurring above 480 nm was attributed to the effect of SPPs traveling at the PTP walls/water interface and contributing to the photocurrent mainly via hot electron injection (Figure 12j).

Fang et al. reported the use of a Fabry–Pérot cavity to enhance the hot electron efficiency in Au–TiO_2–Au films with Antenna-Spacer-Mirror (ASM) geometry.[160] Au antenna disks (height:

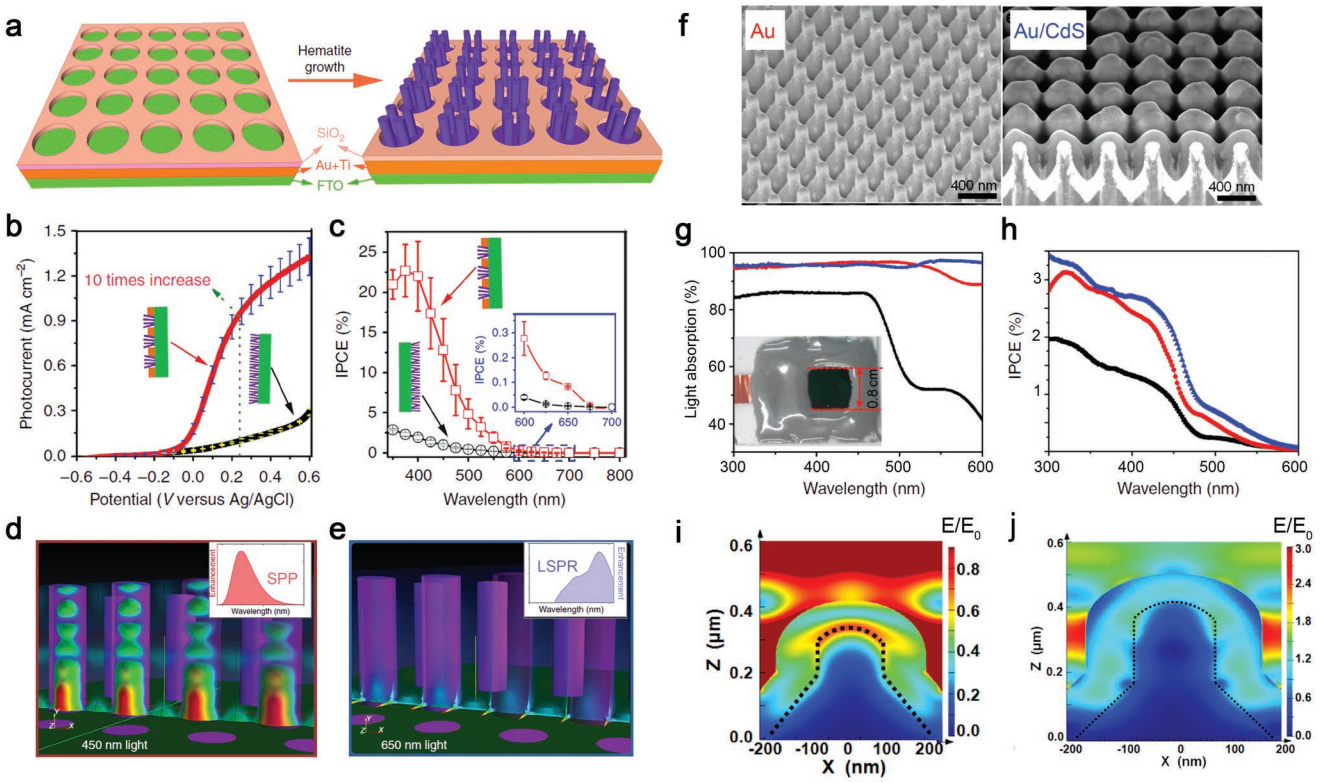

Figure 12. a) Schematics of hematite NRs grown on an Au nanohole array. b) Photocurrent and c) IPCE curves of bare hematite and hematite on an Au nanohole array under 1 Sun illumination. d,e) Finite difference time-domain (FDTD) simulation of SPP launched in the Au nanohole array and absorbed as waveguided modes in hematite NRs (d) and weak LSPR mode localized in the edge of the Au nanoholes (e). f) SEM images of Au truncated pyramid array (PTP) and Au PTP covered with a CdS overlayer. g) Absorption spectra and h) IPCE spectra of CdS/Au PTP (blue line), CdS/Au pillars (red line), and planar CdS/Au (black line). i,j) FDTD-simulated electric field distributions of CdS/Au PTP at wavelengths of 350 nm (i) and 550 nm (j). a–e) Reproduced with permission.[158] Copyright 2013, Nature Publishing Group. f–j) Reproduced with permission.[159] Copyright 2017, American Chemical Society.

35 nm, diameter: 90 nm) were placed on top of a TiO_2 film on an Au layer, which acted as a back mirror. The Au antennas revealed several LSPRs decaying into photons that were then scattered into the semiconductor. The photons bounced back from the Au mirror placed at the bottom, leading to multiple absorption events in the antennas. Owing to hot electron injection from the antennas to the TiO_2 spacer layers, the resulting photocurrent was 2–10 times higher for this structure than that achieved for the one without the back mirror.

Moreover, the electric field enhancement and the hot electron generation may be increased by coupling photonic modes excited in high-index dielectrics to the LSPR. Zhang et al. reported the use of Au–TiO_2 Janus NPs (**Figure 13**a),[161] where the dielectric TiO_2 sphere supported the so-called whispering gallery mode (WGM) resonances. These resonances coupled to and extended the LSPR absorption of Au NPs over the entire visible spectrum, only when TiO_2 NPs in the range of 200–600 nm were considered. Figure 13b shows the electromagnetic field simulation of coupled Au–TiO_2 NPs illuminated by a wavelength of 553 nm. These NPs exhibited different resonances, depending on the different Au decoration, and an overall enhanced absorption cross-section over the visible spectrum (Figure 13c,d). This resulted in a photocurrent enhancement of approximately three times for the best Au–TiO_2 configuration compared to the bare TiO_2 (Figure 13e). The IPCE spectra of Au–TiO_2 were enhanced only in the visible region, consistent with an enhanced hot electron injection mechanism stemming from interactions between WGM and LSPR modes (Figure 13f).

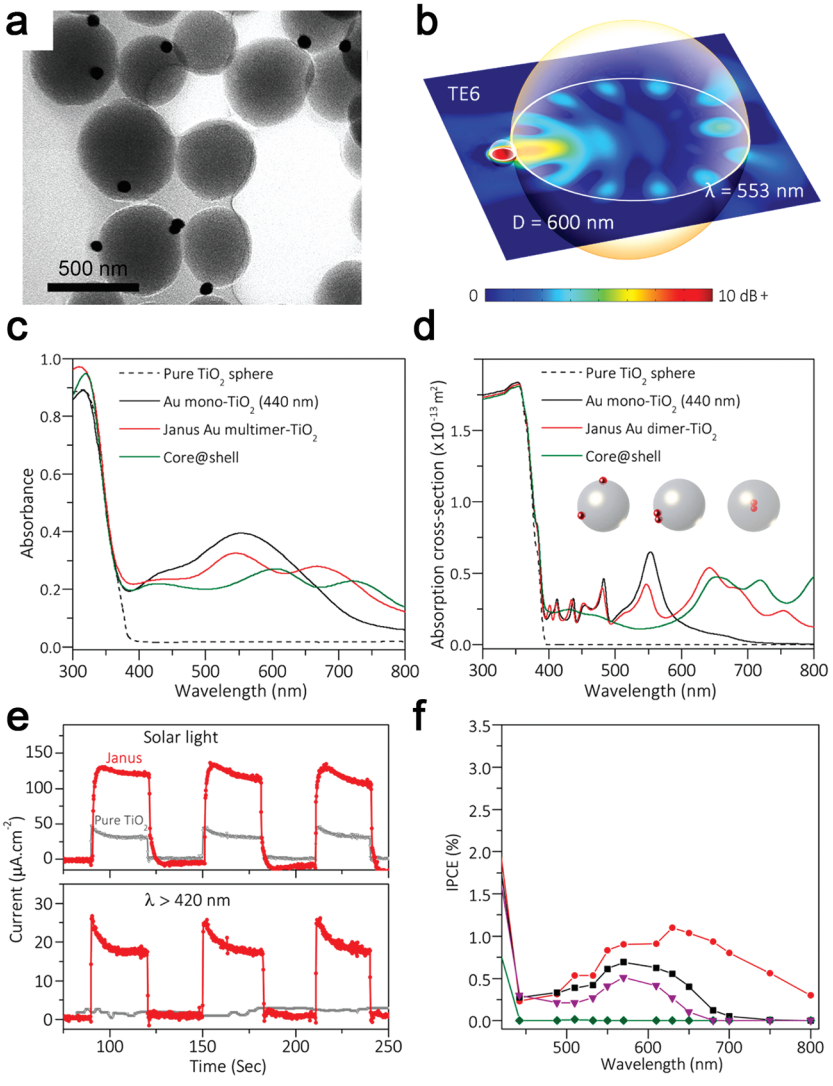

Figure 13. a) TEM image of Au mono–TiO_2 NPs. b) Finite element simulation of an Au mono–TiO_2 NP showing the interplay between the LSPR in the NP and the whispering gallery mode (WGM) resonance in the TiO_2 NP. c) Experimental and d) simulated absorption spectra of pure TiO_2 and Janus Au mono/multimer–TiO_2 particles. e) Chopped photocurrent curves using Janus- and pure TiO_2-based PEC photoelectrodes under full solar (top) and visible-NIR light (bottom) irradiation. f) IPCE spectra of Au–TiO_2 with different morphologies: core–shell (green line), Au mono-TiO_2 (60 nm, purple), Au mono–TiO_2 (440 nm, black), and Janus Au dimer–TiO_2 (red). Reproduced with permission.[161] Copyright 2016, American Chemical Society.

4. Catalytic Effects

Metal NPs have been extensively investigated not only for their plasmonic properties, but also for their catalytic ones. In heterogeneous catalysis, for instance, they lower the activation energy of chemical reactions by providing different mechanistic routes, which begin with the adsorption of molecules on the metal surface.[162] In photocatalysis, metal NPs typically act as co-catalysts on semiconductor NPs, allowing the selective transfer of photogenerated charges, i.e., either electrons or holes, to the electrolyte, reducing the recombination rate and improving the kinetics.[2] In the case of PEC water splitting, similarly, the surface of a photoanode or a photocathode can be modified with OER or HER catalysts, respectively. The first ones are typically oxides (e.g., IrO_2, Co_3O_4, and Co–Pi), the second ones noble metals (e.g., Pt, Pd, and Au).[163,164] Their effect is schematically illustrated in **Figure 14**a: the photocurrent–voltage characteristics of a photoanode with poor surface catalytic activity (blue dotted curve) is compared with that of a material exhibiting an improved performance (red curve). This improvement is reflected in the significant cathodic shift (i.e., to less positive applied potential) of the onset potential (V_{on}) toward the ideal curve (gray dashed line) approaching the flatband potential (V_{fb}). A substantial difference between V_{fb} and V_{on} may also be due to the presence of surface states, leading to Fermi level pinning,[165] as often encountered for hematite (α-Fe_2O_3).[166,167] A possible solution in this case consists of adding oxide passivation layers, such as Al_2O_3, Ga_2O_3, and In_2O_3.[168]

Haro et al. reported a catalytic effect leading to a photocurrent increase of

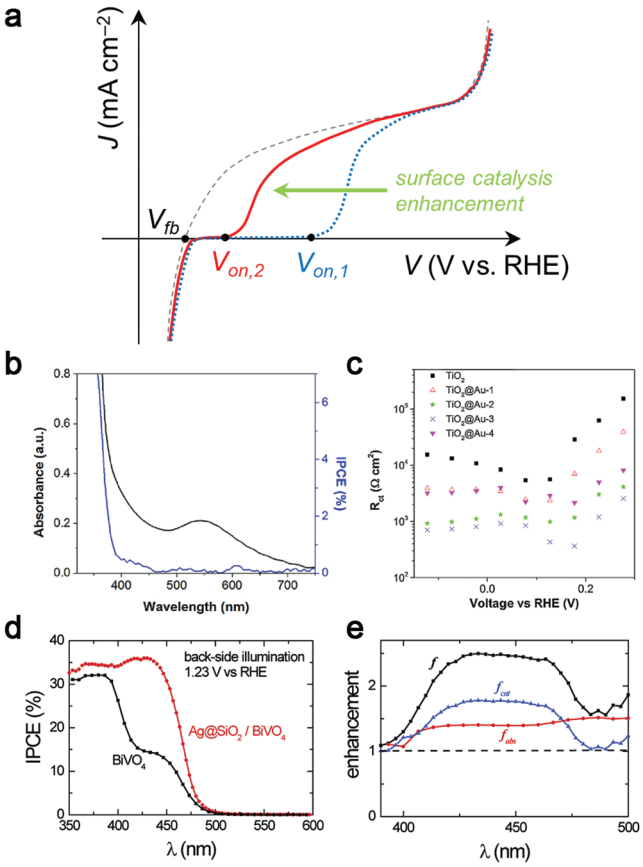

Figure 14. a) Schematic showing the photocurrent-voltage characteristics of a photoanode exhibiting an ideal behavior (Gärtner model,[176] dashed gray line), with a high degree of surface recombination (blue dotted line) and with surface catalysts (red line). b) Absorbance and IPCE spectra of a TiO_2 mesoporous film loaded with Au NPs. c) Charge transfer resistance of mesoporous TiO_2 films with different loadings of Au NPs under illumination at 100 mW cm^{-2}. d) IPCE of bare- and $Ag@SiO_2$–$BiVO_4$ photoanodes obtained with back-side illumination at 1.23 V vs RHE. e) Absorption (f_{abs}), catalytic (f_{cat}), and total (f) enhancement factors of $Ag@SiO_2$–$BiVO_4$ as a function of the excitation wavelength. b,c) Reproduced with permission.[169] Copyright 2014, Elsevier. d,e) Reproduced with permission.[171] Copyright 2014, Royal Society of Chemistry.

mesoporous TiO_2 films loaded with Au NPs, in the absence of hot electron injection.[169] A comparison of the IPCE and the absorption spectra of the Au/TiO_2 revealed that the Au LSPR yielded no enhancement (see Figure 14b). In that work, the charge-transport dynamics in the Au/TiO_2 films was determined by electrochemical impedance spectroscopy (EIS) at different applied potentials under illumination. A decrease of charge-transfer resistance R_{ct} was found for each investigated Au/TiO_2 sample compared to the reference TiO_2 (Figure 14c), thereby elucidating the catalytic role of the Au NPs.

In addition, Wang et al.[170] have employed EIS to elucidate the effect of Au NP decoration on α-Fe_2O_3/FeOOH photoanodes, which exhibited a better PEC response than α-Fe_2O_3/FeOOH, α-Fe_2O_3/Au, and bare α-Fe_2O_3. Also in this case, a clear fingerprint of the Au LSPR was absent in IPCE spectra. A decrease of R_{ct} was found for the α-Fe_2O_3/FeOOH/Au nanoflakes (162 Ω) as compared to the same without Au NPs (256 Ω). Thus, the authors surmised that Au NPs amplified the surface catalytic effect of FeOOH by injecting hot electrons into this layer and enhancing the OER kinetics.

A different strategy to ascertain the catalytic role of plasmonic nanostructures has been reported by Abdi et al.[171] for $BiVO_4$ photoanodes decorated with $Ag@SiO_2$ core–shell NPs. The authors measured the PEC response of these photoanodes and found an IPCE increase for wavelengths between 400 and 500 nm (Figure 14d). However, the photocurrent generated by the composite photoanodes exceeded the value predicted by integrating the calculated absorbance over the AM1.5 irradiance. Therefore, the authors performed a thorough PEC analysis in terms of the so-called enhancement factors. The total enhancement factor, $f(\lambda)$, was defined as

$$f(\lambda) = \frac{J_{NPs}(\lambda)}{J_{bare}(\lambda)} \tag{26}$$

where $J_{NPs}(\lambda)$ and $J_{bare}(\lambda)$ are the photocurrents of $BiVO_4$ with and without $Ag@SiO_2$ NPs, respectively. The same ratio was evaluated after H_2O_2 was added to the electrolyte. H_2O_2 is an effective hole scavenger, which yields unitary charge injection[104] and allows the definition of a photocurrent enhancement that depends only on plasmonic effects:

$$f_{abs}(\lambda) = \frac{J_{NPs}^{H_2O_2}(\lambda)}{J_{bare}^{H_2O_2}(\lambda)} \tag{27}$$

where $J_{NPs}^{H_2O_2}(\lambda)$ and $J_{bare}^{H_2O_2}(\lambda)$ are the photocurrents of $BiVO_4$ with and without $Ag@SiO_2$ NPs, respectively. The catalytic enhancement factor was determined from

$$f_{cat}(\lambda) = f(\lambda)/f_{abs}(\lambda) \tag{28}$$

The enhancement factors obtained from Equations (26–28) (see Figure 14e) revealed a larger catalytic enhancement than the plasmonic one, which was attributed to the electrocatalytic activity of $Ag@SiO_2$ NPs on the surface of $BiVO_4$.

A similar procedure was applied by Valenti et al.[172] for thin (200 nm) $CuWO_4$ photoanodes combined with Au NPs (35 nm diameter).

Finally, plasmonic NPs have also led to an increase in the catalytic activity of electrocatalyst materials, as reported for Au NRs[173] or NPs[174] on MoS_2 and Au-NP-decorated $Ni(OH)_2$.[175]

In the first case, a positive shift of the onset potential (from −0.22 to −0.16 V vs RHE) occurred when the Au–MoS_2 electrode was illuminated with a laser wavelength corresponding to the LSPR. This was attributed to the hot electron injection from Au NRs to the CB of MoS_2, leading to an increase in the Fermi level and a decrease in the overpotential of the semiconductor for the HER.[173] Similarly, in the second case, the resonant illumination of $Ni(OH)_2$–Au composites allowed substantial reduction of the OER overpotential at the current density of 10 mA cm^{-2} (from 330 to 270 mV). This was attributed to an enhanced generation of $Ni^{III/IV}$ active species

(oxidation of Ni^{II} driven by hot holes) and improved charge transfer.[175]

5. All-Plasmonic Hot-Carrier Water Splitting Devices

While in Section 3 we have discussed the mechanisms by which plasmonic nanostructures can enhance the performance of semiconductor photoelectrodes, here we consider the case where charge carriers involved in the PEC process are all originated by plasmon decay.

Figure 15a illustrates this concept for two alternative cases, based on the extraction of hot electrons (left) and hot holes (right) by a Schottky contact. In the first case an n-type semiconductor forms an upward bend-bending in contact with a plasmonic metal, e.g., Au, driving the extraction of hot electrons. Electrons are transported toward the counter electrode to perform the HER, while holes react on the metal surface to drive the OER. Consequently, the device operates as a plasmonic photoanode. Similarly, employing a p-type semiconductor may favor the extraction of hot holes, which are transported away to drive the OER. The electrons remaining on the metal drive the HER and, hence, the device functions as a plasmonic photocathode.[177] In either cases, the semiconductor does not produce charge carriers, but rather it acts as a "filter" for their separation.

Moskovits and co-workers have reported this approach by functionalizing Au NR arrays to employ them as photoanodes, photocathodes or the so-called autonomous photosynthetic devices.[178–180] At first, Au NRs (90 nm diameter) grown on TiO_2-coated FTO substrate were functionalized with TiO_2 (20 nm thickness) on top and a cobalt-based oxygen evolution catalyst (Co-OEC), and were investigated as photoanodes. Maximum photocurrents of 0.1 mA cm^{-2} at 0.5 V vs RHE under AM 1.5G illumination and 0.35 mA cm^{-2} at 1 V vs RHE under visible-light illumination were achieved, while significantly lower values were found under UV illumination or without Co-OEC. The proposed mechanism consisted of hot carrier generation in the Au NRs upon plasmon decay, electron injection in the FTO/TiO_2 substrate, with electrons reaching the Pt cathode for the HER, and hole injection in the Co-OEC, driving the OER.[178] The authors extended their approach by developing an autonomous photosynthetic device, where the overall water splitting reaction occurred in the absence of a counter electrode and an applied bias.[179] This was achieved through the addition of Pt NPs (2 nm diameter) as HER catalysts (Figure 15b), so that hot electrons could move to the TiO_2/Pt cap layer to drive the HER, while the holes were again

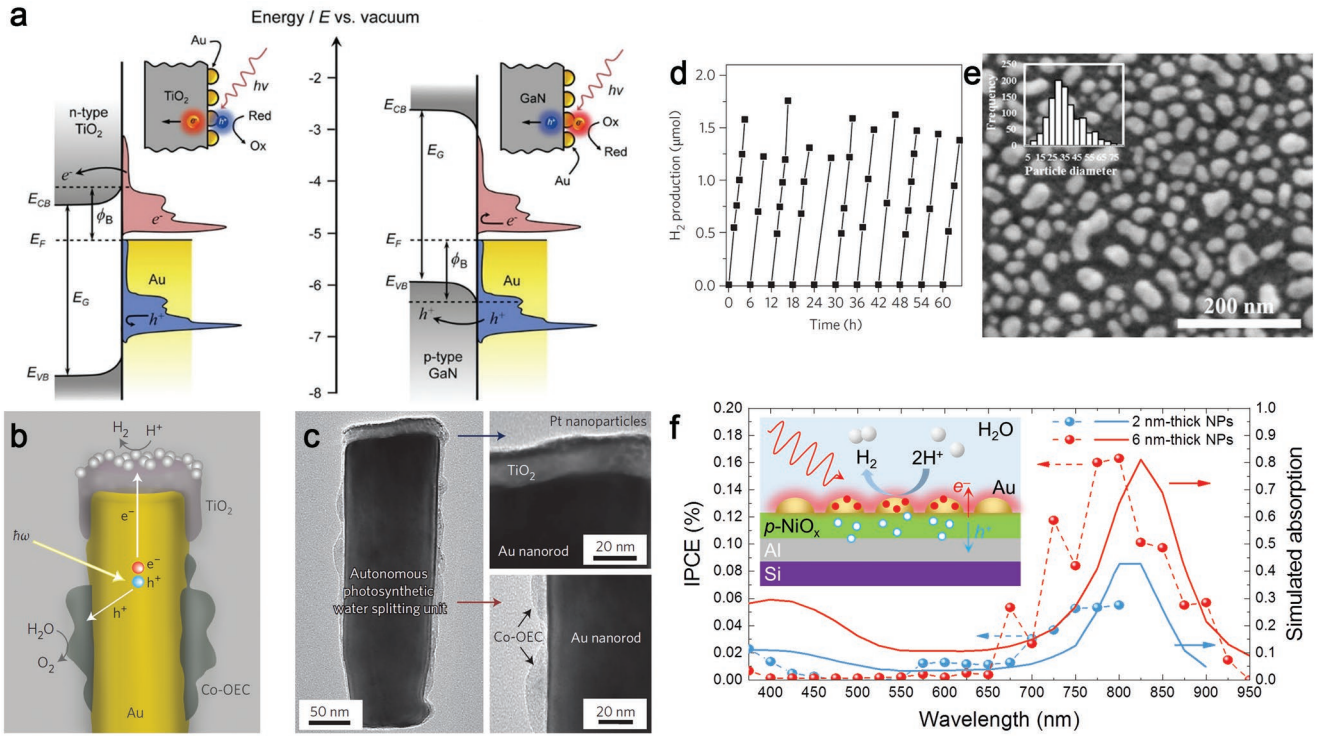

Figure 15. a) Hot carrier collection across a Schottky barrier at metal/n-type semiconductor (left) and metal/p-type semiconductor (right) heterojunctions. E_{CB}: conduction band edge; E_{VB}: valence band edge; E_G: bandgap; E_F: Fermi level; Φ_B: Schottky barrier height. b) Schematic of a photosynthetic unit showing the inner Au NR, the TiO_2 cap decorated with Pt NPs (hydrogen evolution catalysts), and the Co-based material oxygen evolution catalyst (Co-OEC). c) TEM image (left) and magnified views of the Pt/TiO_2 cap (top right) and the Co-OEC (bottom right). d) Hydrogen evolution ($\lambda > 410$ nm) as a function of time (for 6 h cycles). e) SEM image and corresponding particle diameter distribution for Au NPs formed from the deposition of a 6 nm thick Au film. f) IPCE (left axis) and simulated absorbed fraction (right axis) for 2 nm (blue) and 6 nm thick (red) Au NPs on p-NiO_x/Al as plasmonic photocathodes; a schematic of their corresponding working mechanism is shown in the inset. a) Reproduced with permission.[177] Copyright 2018, American Chemical Society. b–d) Reproduced with permission.[179] Copyright 2013, Nature Publishing Group. e,f) Reproduced with permission.[181] Copyright 2015, American Chemical Society.

directed toward the Co-OEC for the OER. Figure 15c shows a transmission electron microscopy (TEM) image of a single functionalized Au NR, where the TiO_2/Pt cap and Co-OEC are positioned in different locations along the NR, yielding spatial separation of the OER and HER sites, respectively. These devices exhibited remarkably stable hydrogen production under visible-light illumination ($\lambda > 410$ nm) at 300 mW cm^{-2} (3 Suns) in 1 M $K_2B_4O_7$ (Figure 15d). An optimum hydrogen production rate and an external quantum efficiency (EQE) of 2.8 mmol h^{-1} g^{-1} and ≈0.25% were realized under these conditions. To confirm the plasmonic mechanism involving only hot carriers, the authors also evaluated the HER by investigating photocathodes prepared from Au NRs without Co-OEC.

Thomann and co-workers developed a different approach toward all-hot carrier photocathodes by designing an Ohmic contact between Au NPs and a p-NiO_x layer.[181] Figure 15e shows a top-view SEM image of the NPs with a broad particle-size distribution (average diameter: ≈30 nm), obtained by annealing a 6 nm thick film. Upon illumination and plasmon excitation, the generated hot electrons were "blocked" on Au NPs, due to the presence of p-NiO_x that functioned as a hole transport layer toward the Al back contact (Figure 15f). Holes were thus transported through an external circuit to a Pt anode to drive the OER, while hot electrons on the NPs reacted directly with the electrolyte, thereby producing H_2. The working mechanism was investigated by comparing IPCE spectra of devices with 2 nm and 6 nm thick Au NPs to the FDTD-simulated absorption spectra (Figure 15f). Figure 15f reveals a qualitatively good agreement between the two datasets, suggesting a fundamental role of the plasmonic charge carriers in the photocurrent generation. The figure also shows that the LSPR of the Au/p-NiO_x photocathodes occurs in the wavelength range 800–825 nm, thereby producing hot electrons with maximum energy of ≈1.55 eV capable of driving the HER. The authors reported a photocurrent of 25 μA cm^{-2} at 0 V vs RHE under 1 Sun illumination and internal quantum efficiency (IQE) of ≈0.2% for the best photocathodes.

Gómez et al. have reported a similar architecture.[182] In that work, an Au (200 nm thick)/TiO_2 (50 nm)/Au NP (20 nm diameter) multilayer photoanode allowed the broadband (600–1000 nm) extraction of hot electrons from the Au NPs to the underlying layers. These electrons eventually reached a Pt cathode to drive the HER, and hot holes were scavenged by adding methanol in the electrolyte. Illumination with $\lambda > 495$ nm yielded a photocurrent of 0.65 μA cm^{-2} and a maximum IPCE of 0.27% at 600 nm, 20 times higher than that of a TiO_2/Au NP device without an underlying thick Au mirror.

Finally, Atwater and co-workers have recently designed a photocathode for CO_2 reduction based on Au NPs forming a Schottky contact with *p*-GaN.[177] This was motivated by the premise of selectively probing the hot holes formed by plasmon decay. In materials like Au, these holes are "hotter" (i.e., having higher energy and, hence, a strong oxidizing power) than hot electrons resulting from the asymmetry in the charge energy distribution (Figure 15a).[119,121] The photocathode exhibited a plasmon resonance at ≈570 nm and a Schottky barrier height of 1.1 eV. The effective extraction of energetic hot holes was confirmed by comparing PEC measurements performed under the same conditions (visible-light illumination with $\lambda > 495$ nm, 5×10^{-4} M K_2CO_3 electrolyte) for Au/p-GaN and Au/p-NiO_x photocathodes: photocurrent values of 1.3 μA cm^{-2} and 2.7 μA cm^{-2} at −0.4 V versus RHE were obtained respectively for the former and for the latter, which forms an Ohmic contact with Au, suggesting that most hot holes could be collected.[177]

6. Conclusions and Perspectives

Despite decades of research on PEC water splitting, the large-scale development of this technology has been hindered by the lack of suitable materials that simultaneously satisfy all the requirements for efficient (≈10%) and stable hydrogen production.

The introduction of plasmonic nanostructures has emerged in the last 10 years as a promising strategy for enhancing the properties of semiconductor photoelectrodes, specifically addressing several shortcomings of earth-abundant materials, thereby resulting in increased efficiencies.

Indirect hot electron injection has been extensively investigated, thereby enabling the visible-light activation of wide-bandgap materials such as TiO_2 and ZnO. Nevertheless, the photocurrents measured under visible light are still on the order of tens–hundreds of μA cm^{-2}, which is still significantly lower than that required for large-scale development. Major developments from both a theoretical and fabrication point of view are necessary for improving the efficiency and justifying the use of this approach in practical devices. The potential of the direct injection mechanism has not been fully disclosed yet due to its recent understanding, but may be much greater considering that the direct process has orders of magnitude higher efficiency than the indirect one.

On the other hand, the PIRET mechanism has led to photocurrents on the order of several mA cm^{-2} for semiconductors with lower bandgap than TiO_2, such as α-Fe_2O_3 and $BiVO_4$. PIRET requires essentially only a good spectral overlap between the plasmonic unit and the semiconductor and may be conveniently combined with scattering and/or photonic modes to achieve high-performance PEC devices. Therefore, we foresee significant development in the use of photonic modes for enhancing PEC water splitting. This development may allow the combination of low-loss photonic modes using high-index dielectrics to surface plasmon resonance, thereby pushing the limit of PEC devices toward market-competitive efficiencies.

We have also considered the catalytic and thermal effects of plasmonic metal NPs, which have often been overlooked in previous studies as they are not correlated with enhanced charge-carrier generation in the semiconductor photoelectrode. Nonetheless, preliminary investigations on these effects (especially for thermoplasmonic effects) have suggested that they may offer a general approach to be routinely used in any PEC device.

The results obtained so far, although remarkable, are still insufficient for meeting all the requirements for practical implementation in a PEC water splitting device. Some of the conceivable directions of development can be envisioned, especially

regarding plasmonic materials. First, compared to those currently available, more efficient, scalable, and cheap processes for the production of plasmonic units and their integration in photoelectrodes should be achieved. Multistep and time-consuming processes should be avoided, and a full CMOS compatibility should be realized. Second, earth-abundant alternative materials to coinage metals, such as Al, metal alloys, metal nitrides (TiN, ZrN), MXenes, or highly doped semiconductors (Ta-doped TiO_2, Al-doped ZnO), should be thoroughly considered. TiN, for example, has already been employed to substitute Au, owing to its plasmon resonance in the visible range. Other nitrides or doped semiconductors with NIR absorption could be used to generate thermal effects. Therefore, a careful combination of different materials could lead to highly efficient and broadband solar light absorption that triggers multiple plasmonic mechanisms within the same device. Third, an improved understanding of the plasmonic mechanisms is required, especially considering the charge-transfer processes between the plasmonic unit and the semiconductor. This is particularly evident for the so-called direct electron injection mechanism, which has been confirmed by experiments only recently. In this regard, the role of Au and Ag can still be relevant, as they would be suitable for proof-of-concept studies thanks to their well-known properties. The direct observation of the plasmonic effects under operational conditions will also play a central role in the development of PEC devices, with PEC microscopy, synchrotron techniques, and ultrafast optical spectroscopy methods being crucial for a decisive leap toward the integration of plasmonic components in real PEC devices for renewable-energy storage.

Acknowledgements

The authors gratefully acknowledge the support by the Operational Programme Research, Development and Education—European Regional Development Fund, projects no. CZ.02.1.01/0.0/0.0/15_003/0000416 and CZ.02.1.01/0.0/0.0/16_019/0000754 of the Ministry of Education, Youth and Sports of the Czech Republic. The authors would also like to acknowledge support from the Air Force Office of Scientific Research grant (FA9550-17-1-0243).

Conflict of Interest

The authors declare no conflict of interest.

Keywords

hydrogen production, photoelectrochemistry, photonic nanostructures, surface plasmons, water splitting

Received: August 24, 2018
Revised: November 23, 2018
Published online:

[1] A. Fujishima, K. Honda, *Nature* **1972**, *238*, 37.
[2] M. G. Walter, E. L. Warren, J. R. McKone, S. W. Boettcher, Q. Mi, E. A. Santori, N. S. Lewis, *Chem. Rev.* **2010**, *110*, 6446.
[3] F. E. Osterloh, *Chem. Soc. Rev.* **2013**, *42*, 2294.
[4] M. Grätzel, *Nature* **2001**, *414*, 338.
[5] J. L. Young, M. A. Steiner, H. Döscher, R. M. France, J. A. Turner, T. G. Deutsch, *Nat. Energy* **2017**, *2*, 17028.
[6] E. Verlage, S. Hu, R. Liu, R. J. R. Jones, K. Sun, C. Xiang, N. S. Lewis, H. A. Atwater, *Energy Environ. Sci.* **2015**, *8*, 3166.
[7] W.-H. Cheng, M. H. Richter, M. M. May, J. Ohlmann, D. Lackner, F. Dimroth, T. Hannappel, H. A. Atwater, H.-J. Lewerenz, *ACS Energy Lett.* **2018**, *3*, 1795.
[8] S. Hu, M. R. Shaner, J. A. Beardslee, M. Lichterman, B. S. Brunschwig, N. S. Lewis, *Science* **2014**, *344*, 1005.
[9] K. Sun, F. H. Saadi, M. F. Lichterman, W. G. Hale, H.-P. Wang, X. Zhou, N. T. Plymale, S. T. Omelchenko, J.-H. He, K. M. Papadantonakis, B. S. Brunschwig, N. S. Lewis, *Proc. Natl. Acad. Sci. USA* **2015**, *112*, 3612.
[10] J. H. Kim, J.-W. Jang, Y. H. Jo, F. F. Abdi, Y. H. Lee, R. van de Krol, J. S. Lee, *Nat. Commun.* **2016**, *7*, 13380.
[11] H.-J. Ahn, A. Goswami, F. Riboni, S. Kment, A. Naldoni, S. Mohajernia, R. Zboril, P. Schmuki, *ChemSusChem* **2018**, *11*, 1873.
[12] I. Cesar, K. Sivula, A. Kay, R. Zboril, M. Grätzel, *J. Phys. Chem. C* **2009**, *113*, 772.
[13] S. Kment, P. Schmuki, Z. Hubicka, L. Machala, R. Kirchgeorg, N. Liu, L. Wang, K. Lee, J. Olejnicek, M. Cada, I. Gregora, R. Zboril, *ACS Nano* **2015**, *9*, 7113.
[14] K. Sivula, R. Zboril, F. Le Formal, R. Robert, A. Weidenkaff, J. Tucek, J. Frydrych, M. Grätzel, *J. Am. Chem. Soc.* **2010**, *132*, 7436.
[15] S. Kment, F. Riboni, S. Pausova, L. Wang, L. Wang, H. Han, Z. Hubicka, J. Krysa, P. Schmuki, R. Zboril, *Chem. Soc. Rev.* **2017**, *46*, 3716.
[16] M. L. Brongersma, N. J. Halas, P. Nordlander, *Nat. Nanotechnol.* **2015**, *10*, 25.
[17] P. Zhang, T. Wang, J. Gong, *Adv. Mater.* **2015**, *27*, 5328.
[18] M. Valenti, M. P. Jonsson, G. Biskos, A. Schmidt-Ott, W. A. Smith, *J. Mater. Chem. A* **2016**, *4*, 17891.
[19] S. K. Cushing, N. Wu, *J. Phys. Chem. Lett.* **2016**, *7*, 666.
[20] T. Tatsuma, H. Nishi, T. Ishida, *Chem. Sci.* **2017**, *8*, 3325.
[21] N. Wu, *Nanoscale* **2018**, *10*, 2679.
[22] Z. Zheng, W. Xie, B. Huang, Y. Dai, *Chem. - Eur. J.* **2018**, *24*, 18322.
[23] K. Sivula, R. van de Krol, *Nat. Rev. Mater.* **2016**, *1*, 15010.
[24] N. W. Ashcroft, N. D. Mermin, *Solid State Physics*, Holt Rinehart & Winston, New York **1976**.
[25] S. A. Maier, *Plasmonics: Fundamentals and Applications*, Springer Science & Business Media, Berlin, Germany **2007**.
[26] W. L. Barnes, *J. Opt. A: Pure Appl. Opt.* **2006**, *8*, S87.
[27] P. Berini, *Adv. Opt. Photonics* **2009**, *1*, 484.
[28] C. F. Bohren, D. R. Huffman, *Absorption and Scattering of Light by Small Particles*, John Wiley & Sons, New York, USA **2008**.
[29] P. K. Jain, K. S. Lee, I. H. El-Sayed, M. A. El-Sayed, *J. Phys. Chem. B* **2006**, *110*, 7238.
[30] G. Mie, *Ann. Phys.* **1908**, *330*, 377.
[31] K. L. Kelly, E. Coronado, L. L. Zhao, G. C. Schatz, *J. Phys. Chem. B* **2003**, *107*, 668.
[32] S. Linic, P. Christopher, D. B. Ingram, *Nat. Mater.* **2011**, *10*, 911.
[33] A. Derkachova, K. Kolwas, I. Demchenko, *Plasmonics* **2016**, *11*, 941.
[34] T. Klar, M. Perner, S. Grosse, G. von Plessen, W. Spirkl, J. Feldmann, *Phys. Rev. Lett.* **1998**, *80*, 4249.
[35] C. Sönnichsen, T. Franzl, T. Wilk, G. von Plessen, J. Feldmann, O. Wilson, P. Mulvaney, *Phys. Rev. Lett.* **2002**, *88*, 077402.
[36] S. K. Cushing, J. Li, F. Meng, T. R. Senty, S. Suri, M. Zhi, M. Li, A. D. Bristow, N. Wu, *J. Am. Chem. Soc.* **2012**, *134*, 15033.
[37] J. Li, S. K. Cushing, F. Meng, T. R. Senty, A. D. Bristow, N. Wu, *Nat. Photonics* **2015**, *9*, 601.
[38] T. Hertel, E. Knoesel, M. Wolf, G. Ertl, *Phys. Rev. Lett.* **1996**, *76*, 535.

[39] F. Ladstädter, U. Hohenester, P. Puschnig, C. Ambrosch-Draxl, *Phys. Rev. B* **2004**, *70*, 235125.
[40] H. Inouye, K. Tanaka, I. Tanahashi, K. Hirao, *Phys. Rev. B* **1998**, *57*, 11334.
[41] M. Lisowski, P. A. Loukakos, U. Bovensiepen, J. Stähler, C. Gahl, M. Wolf, *Appl. Phys. A: Mater. Sci. Process.* **2004**, *78*, 165.
[42] S. Link, M. A. El-Sayed, *J. Phys. Chem. B* **1999**, *103*, 8410.
[43] C. Voisin, N. Del Fatti, D. Christofilos, F. Vallée, *J. Phys. Chem. B* **2001**, *105*, 2264.
[44] G. Baffou, R. Quidant, *Laser Photonics Rev.* **2013**, *7*, 171.
[45] G. Baffou, C. Girard, R. Quidant, *Phys. Rev. Lett.* **2010**, *104*, 136805.
[46] Z. Chen, X. Shan, Y. Guan, S. Wang, J.-J. Zhu, N. Tao, *ACS Nano* **2015**, *9*, 11574.
[47] T. Bora, D. Zoepfl, J. Dutta, *Sci. Rep.* **2016**, *6*, 26913.
[48] A. Furube, L. Du, K. Hara, R. Katoh, M. Tachiya, *J. Am. Chem. Soc.* **2007**, *129*, 14852.
[49] L. Du, A. Furube, K. Yamamoto, K. Hara, R. Katoh, M. Tachiya, *J. Phys. Chem. C* **2009**, *113*, 6454.
[50] R. Long, O. V. Prezhdo, *J. Am. Chem. Soc.* **2014**, *136*, 4343.
[51] K. Wu, J. Chen, J. R. McBride, T. Lian, *Science* **2015**, *349*, 632.
[52] A. Huck, S. Smolka, P. Lodahl, A. S. Sorenson, A. Boltasseva, J. Janousek, U. L. Anderson, *Phys. Rev. Lett.* **2009**, *102*, 246801.
[53] K.-C. Li, H.-C. Chu, Y. Lin, H.-Y. Tuan, Y.-C. Hu, *ACS Appl. Mater. Interfaces* **2016**, *8*, 12082.
[54] C. Delacour, S. Blaize, P. Grosse, J. M. Fedeli, A. Bruyant, R. Salas-Montiel, G. Lerondel, A. Chelnokov, *Nano Lett.* **2010**, *10*, 2922.
[55] D. Y. Fedyanin, D. I. Yakubovsky, R. V. Kirtaev, V. S. Volkov, *Nano Lett.* **2016**, *16*, 362.
[56] Q.-C. Sun, Y. Ding, S. M. Goodman, H. H. Funke, P. Nagpal, *Nanoscale* **2014**, *6*, 12450.
[57] J. T. Kim, J. J. Ju, S. Park, M. Kim, S. K. Park, M.-H. Lee, *Opt. Express* **2008**, *16*, 13133.
[58] Y.-J. Lu, J. Kim, H.-Y. Chen, C. Wu, N. Dabidian, C. E. Sanders, C.-Y. Wang, M.-Y. Lu, B.-H. Li, X. Qiu, W.-H. Chang, L.-J. Chen, G. Shvets, C.-K. Shih, S. Gwo, *Science* **2012**, *337*, 450.
[59] V. Amendola, R. Pilot, M. Frasconi, O. M. Maragò, M. A. Iatì, *J. Phys.: Condens. Matter* **2017**, *29*, 203002.
[60] L. Sun, C. Zhang, C.-Y. Wang, P.-H. Su, M. Zhang, S. Gwo, C.-K. Shih, X. Li, Y. Wu, *Sci. Rep.* **2017**, *7*, 8917.
[61] M. W. Knight, N. S. King, L. Liu, H. O. Everitt, P. Nordlander, N. J. Halas, *ACS Nano* **2014**, *8*, 834.
[62] S. Ramadurgam, T.-G. Lin, C. Yang, *Nano Lett.* **2014**, *14*, 4517.
[63] D. F. Swearer, H. Zhao, L. Zhou, C. Zhang, H. Robatjazi, J. M. P. Martirez, C. M. Krauter, S. Yazdi, M. J. McClain, E. Ringe, E. A. Carter, P. Nordlander, N. J. Halas, *Proc. Natl. Acad. Sci. USA* **2016**, *113*, 8916.
[64] G. Albrecht, S. Kaiser, H. Giessen, M. Hentschel, *Nano Lett.* **2017**, *17*, 6402.
[65] G. Baraldi, M. Carrada, J. Toudert, F. J. Ferrer, A. Arbouet, V. Paillard, J. Gonzalo, *J. Phys. Chem. C* **2013**, *117*, 9431.
[66] P. R. West, S. Ishii, G. V. Naik, N. K. Emani, V. M. Shalaev, A. Boltasseva, *Laser Photonics Rev.* **2010**, *4*, 795.
[67] G. V. Naik, V. M. Shalaev, A. Boltasseva, *Adv. Mater.* **2013**, *25*, 3264.
[68] G. V Naik, J. L. Schroeder, X. Ni, A. V. Kilidshev, T. D. Sands, A. Boltasseva, *Opt. Mater. Express* **2012**, *2*, 478.
[69] U. Guler, G. V. Naik, A. Boltasseva, V. M. Shalaev, A. V. Kildishev, *Appl. Phys. B* **2012**, *107*, 285.
[70] S. Ishii, R. P. Sugavaneshwar, T. Nagao, *J. Phys. Chem. C* **2016**, *120*, 2343.
[71] J. A. Briggs, G. V. Naik, T. A. Petach, B. K. Baum, D. Goldhaber-Gordon, J. A. Dionne, *Appl. Phys. Lett.* **2016**, *108*, 051110.
[72] U. Guler, J. C. Ndukaife, G. V. Naik, A. G. A. Nnanna, A. V. Kildishev, V. M. Shalaev, A. Boltasseva, *Nano Lett.* **2013**, *13*, 6078.
[73] J. Hu, X. Ren, A. N. Reed, T. Reese, D. Rhee, B. Howe, L. J. Lauhon, A. M. Urbas, T. W. Odom, *ACS Photonics* **2017**, *4*, 606.
[74] A. Lalisse, G. Tessier, J. Plain, G. Baffou, *Sci. Rep.* **2016**, *6*, 38647.
[75] M. Chirumamilla, A. Chirumamilla, Y. Yang, A. S. Roberts, P. K. Kristensen, K. Chaudhuri, A. Boltasseva, D. S. Sutherland, S. I. Bozhevolnyi, K. Pedersen, *Adv. Opt. Mater.* **2017**, *5*, 1700552.
[76] Z. W. Seh, K. D. Fredrickson, B. Anasori, J. Kibsgaard, A. L. Strickler, M. R. Lukatskaya, Y. Gogotsi, T. F. Jaramillo, A. Vojvodic, *ACS Energy Lett.* **2016**, *1*, 589.
[77] B. Anasori, M. R. Lukatskaya, Y. Gogotsi, *Nat. Rev. Mater.* **2017**, *2*, 16098.
[78] H. Wang, Y. Wu, X. Yuan, G. Zeng, J. Zhou, X. Wang, J. W. Chew, *Adv. Mater.* **2018**, *30*, 1704561.
[79] X. Jiang, S. Liu, W. Liang, S. Luo, Z. He, Y. Ge, H. Wang, R. Cao, F. Zhang, Q. Wen, J. Li, Q. Bao, D. Fan, H. Zhang, *Laser Photonics Rev.* **2018**, *12*, 1700229.
[80] K. Chaudhuri, M. Alhabeb, Z. Wang, V. M. Shalaev, Y. Gogotsi, A. Boltasseva, *ACS Photonics* **2018**, *5*, 1115.
[81] K. Diest, V. Liberman, D. M. Lennon, P. B. Welander, M. Rothschild, *Opt. Express* **2013**, *21*, 28638.
[82] P. B. Johnson, R. W. Christy, *Phys. Rev. B* **1972**, *6*, 4370.
[83] K. M. McPeak, S. V. Jayanti, S. J. P. Kress, S. Meyer, S. Iotti, A. Rossinelli, D. J. Norris, *ACS Photonics* **2015**, *2*, 326.
[84] J.-H. Li, M. Hayashi, G.-Y. Guo, *Phys. Rev. B* **2013**, *88*, 155437.
[85] J. S. Biggins, S. Yazdi, E. Ringe, *Nano Lett.* **2018**, *18*, 3752.
[86] C. J. Powell, J. B. Swan, *Phys. Rev.* **1959**, *116*, 81.
[87] Y. Zhao, C. Burda, *Energy Environ. Sci.* **2012**, *5*, 5564.
[88] J. Kim, G. V. Naik, A. V. Gavrilenko, K. Dondapati, V. I. Gavrilenko, S. M. Prokes, O. J. Glembocki, V. M. Shalaev, A. Boltasseva, *Phys. Rev. X* **2014**, *3*, 1.
[89] S. Q. Li, P. Guo, L. Zhang, W. Zhou, T. W. Odom, T. Seideman, J. B. Ketterson, R. P. H. Chang, *ACS Nano* **2011**, *5*, 9161.
[90] T. Förster, *Die Naturwiss.* **1946**, *33*, 166.
[91] T. Förster, *Ann. Phys.* **1948**, *437*, 55.
[92] J. R. Lakowicz, *Principles of Fluorescence Spectroscopy*, 3rd ed., Springer, Berlin, Germany **2006**.
[93] D. B. Ingram, S. Linic, *J. Am. Chem. Soc.* **2011**, *133*, 5202.
[94] Z. Liu, W. Hou, P. Pavaskar, M. Aykol, S. B. Cronin, *Nano Lett.* **2011**, *11*, 1111.
[95] E. Thimsen, F. Le Formal, M. Grätzel, S. C. Warren, *Nano Lett.* **2011**, *11*, 35.
[96] Y.-C. Pu, G. Wang, K.-D. Chang, Y. Ling, Y.-K. Lin, B. C. Fitzmorris, C.-M. Liu, X. Lu, Y. Tong, J. Z. Zhang, Y.-J. Hsu, Y. Li, *Nano Lett.* **2013**, *13*, 3817.
[97] J. S. DuChene, B. P. Williams, A. C. Johnston-Peck, J. Qiu, M. Gomes, M. Amilhau, D. Bejleri, J. Weng, D. Su, F. Huo, E. A. Stach, W. D. Wei, *Adv. Energy Mater.* **2016**, *6*, 1501250.
[98] J. K. Kim, X. Shi, M. J. Jeong, J. Park, H. S. Han, S. H. Kim, Y. Guo, T. F. Heinz, S. Fan, C.-L. Lee, J. H. Park, X. Zheng, *Adv. Energy Mater.* **2018**, *8*, 1701765.
[99] M. G. Lee, C. W. Moon, H. Park, W. Sohn, S. B. Kang, S. Lee, K. J. Choi, H. W. Jang, *Small* **2017**, *13*, 1701644.
[100] I. Thomann, B. A. Pinaud, Z. Chen, B. M. Clemens, T. F. Jaramillo, M. L. Brongersma, *Nano Lett.* **2011**, *11*, 3440.
[101] U. Kreibig, M. Vollmer, *Optical Properties of Metal Clusters*, Springer, Berlin, Germany **1995**.
[102] H. A. Atwater, A. Polman, *Nat. Mater.* **2010**, *9*, 205.
[103] M. Valenti, E. Kontoleta, I. A. Digdaya, M. P. Jonsson, G. Biskos, A. Schmidt-Ott, W. A. Smith, *ChemNanoMat* **2016**, *2*, 739.
[104] H. Dotan, K. Sivula, M. Grätzel, A. Rothschild, S. C. Warren, *Energy Environ. Sci.* **2011**, *4*, 958.

[105] L. Zhang, L. O. Herrmann, J. J. Baumberg, *Sci. Rep.* **2015**, *5*, 16660.
[106] P. Peerakiatkhajohn, T. Butburee, J.-H. Yun, H. Chen, R. M. Richards, L. Wang, *J. Mater. Chem. A* **2015**, *3*, 20127.
[107] P. S. Archana, N. Pachauri, Z. Shan, S. Pan, A. Gupta, *J. Phys. Chem. C* **2015**, *119*, 15506.
[108] W. Schottky, *Z. Phys.* **1939**, *113*, 367.
[109] N. F. Mott, *Proc. R. Soc. A* **1939**, *171*, 27.
[110] R. T. Tung, *Appl. Phys. Rev.* **2014**, *1*, 011304.
[111] A. Naldoni, U. Guler, Z. Wang, M. Marelli, F. Malara, X. Meng, L. V. Besteiro, A. O. Govorov, A. V. Kildishev, A. Boltasseva, V. M. Shalaev, *Adv. Opt. Mater.* **2017**, *5*, 1601031.
[112] S.-F. Hung, F.-X. Xiao, Y.-Y. Hsu, N.-T. Suen, H.-B. Yang, H. M. Chen, B. Liu, *Adv. Energy Mater.* **2016**, *6*, 1501339.
[113] M. W. Knight, H. Sobhani, P. Nordlander, N. J. Halas, *Science* **2011**, *332*, 702.
[114] J. Sá, G. Tagliabue, P. Friedli, J. Szlachetko, M. H. Rittmann-Frank, F. G. Santomauro, C. J. Milne, H. Sigg, *Energy Environ. Sci.* **2013**, *6*, 3584.
[115] C. R. Crowell, W. G. Spitzer, L. E. Howarth, E. E. LaBate, *Phys. Rev.* **1962**, *127*, 2006.
[116] R. H. Fowler, *Phys. Rev.* **1931**, *38*, 45.
[117] Y. K. Lee, C. H. Jung, J. Park, H. Seo, G. A. Somorjai, J. Y. Park, *Nano Lett.* **2011**, *11*, 4251.
[118] L. V. Besteiro, X.-T. Kong, Z. Wang, G. Hartland, A. O. Govorov, *ACS Photonics* **2017**, *4*, 2759.
[119] A. O. Govorov, H. Zhang, Y. K. Gun'ko, *J. Phys. Chem. C* **2013**, *117*, 16616.
[120] H. Zhang, A. O. Govorov, *J. Phys. Chem. C* **2014**, *118*, 7606.
[121] A. M. Brown, R. Sundararaman, P. Narang, W. A. Goddard, H. A. Atwater, *ACS Nano* **2016**, *10*, 957.
[122] R. Sundararaman, P. Narang, A. S. Jermyn, W. A. G. III, H. A. Atwater, *Nat. Commun.* **2014**, *5*, 5788.
[123] A. Manjavacas, J. G. Liu, V. Kulkarni, P. Nordlander, *ACS Nano* **2014**, *8*, 7630.
[124] M. Bernardi, J. Mustafa, J. B. Neaton, S. G. Louie, *Nat. Commun.* **2015**, *6*, 7044.
[125] S. Dal Forno, L. Ranno, J. Lischner, *J. Phys. Chem. C* **2018**, *122*, 8517.
[126] G. V. Hartland, L. V. Besteiro, P. Johns, A. O. Govorov, *ACS Energy Lett.* **2017**, *2*, 1641.
[127] S. K. Cushing, C.-J. Chen, C. L. Dong, X.-T. Kong, A. O. Govorov, R.-S. Liu, N. Wu, *ACS Nano* **2018**, *12*, 7117.
[128] S. Tan, A. Argondizzo, J. Ren, L. Liu, J. Zhao, H. Petek, *Nat. Photonics* **2017**, *11*, 806.
[129] Y. Tian, T. Tatsuma, *J. Am. Chem. Soc.* **2005**, *127*, 7632.
[130] Y. Nishijima, K. Ueno, Y. Yokota, K. Murakoshi, H. Misawa, *J. Phys. Chem. Lett.* **2010**, *1*, 2031.
[131] L. Amidani, A. Naldoni, M. Malvestuto, M. Marelli, P. Glatzel, V. Dal Santo, F. Boscherini, *Angew. Chem., Int. Ed.* **2015**, *54*, 5413.
[132] H. M. Chen, C. K. Chen, C.-J. Chen, L.-C. Cheng, P. C. Wu, B. H. Cheng, Y. Z. Ho, M. L. Tseng, Y.-Y. Hsu, T.-S. Chan, J.-F. Lee, R.-S. Liu, D. P. Tsai, *ACS Nano* **2012**, *6*, 7362.
[133] A. Mang, K. Reimann, S. Rübenacke, *Solid State Commun.* **1995**, *94*, 251.
[134] Y. Mi, L. Wen, R. Xu, Z. Wang, D. Cao, Y. Fang, Y. Lei, *Adv. Energy Mater.* **2016**, *6*, 1501496.
[135] X. Zhang, Y. Liu, Z. Kang, *ACS Appl. Mater. Interfaces* **2014**, *6*, 4480.
[136] X. Zhang, Y. Liu, S.-T. Lee, S. Yang, Z. Kang, *Energy Environ. Sci.* **2014**, *7*, 1409.
[137] Z. Zhang, L. Zhang, M. N. Hedhili, H. Zhang, P. Wang, *Nano Lett.* **2013**, *13*, 14.
[138] P. Peerakiatkhajohn, J.-H. Yun, H. Chen, M. Lyu, T. Butburee, L. Wang, *Adv. Mater.* **2016**, *28*, 6405.
[139] U. Guler, V. M. Shalaev, A. Boltasseva, *Mater. Today* **2015**, *18*, 227.
[140] A. O. Govorov, H. H. Richardson, *Nano Today* **2007**, *2*, 30.
[141] A. Naldoni, V. M. Shalaev, M. L. Brongersma, *Science* **2017**, *356*, 908.
[142] S. Licht, *Electrochem. Commun.* **2002**, *4*, 790.
[143] Y. Pihosh, I. Turkevych, K. Mawatari, J. Uemura, Y. Kazoe, S. Kosar, K. Makita, T. Sugaya, T. Matsui, D. Fujita, *Sci. Rep.* **2015**, *5*, 11141.
[144] X. Ye, J. Yang, M. Boloor, N. A. Melosh, W. C. Chueh, *J. Mater. Chem. A* **2015**, *3*, 10801.
[145] L. Zhang, X. Ye, M. Boloor, A. Poletayev, N. A. Melosh, W. C. Chueh, *Energy Environ. Sci.* **2016**, *9*, 2044.
[146] L. Zhang, L. Sun, Z. Guan, S. Lee, Y. Li, H. D. Deng, Y. Li, N. L. Ahlborg, M. Boloor, N. A. Melosh, W. C. Chueh, *Nano Lett.* **2017**, *17*, 5264.
[147] D. Agarwal, C. O. Aspetti, M. Cargnello, M. Ren, J. Yoo, C. B. Murray, R. Agarwal, *Nano Lett.* **2017**, *17*, 1839.
[148] C. Wang, O. Ranasingha, S. Natesakhawat, P. R. Ohodnicki, M. Andio, J. P. Lewis, C. Matranga, *Nanoscale* **2013**, *5*, 6968.
[149] M. Balkanski, R. F. Wallis, E. Haro, *Phys. Rev. B* **1983**, *28*, 1928.
[150] R. Cuscó, E. Alarcón-Lladó, J. Ibáñez, L. Artús, J. Jiménez, B. Wang, M. J. Callahan, *Phys. Rev. B* **2007**, *75*, 165202.
[151] H. Kumar Yadav, R. S. Katiyar, V. Gupta, *Appl. Phys. Lett.* **2012**, *100*, 051906.
[152] T. Ohsaka, *J. Phys. Soc. Jpn.* **1980**, *48*, 1661.
[153] Y. L. Du, Y. Deng, M. S. Zhang, *J. Phys. Chem. Solids* **2006**, *67*, 2405.
[154] R. C. Prince, R. R. Frontiera, E. O. Potma, *Chem. Rev.* **2017**, *117*, 5070.
[155] E. L. Keller, R. R. Frontiera, *ACS Nano* **2018**, *12*, 5848.
[156] Y. Yu, V. Sundaresan, K. A. Willets, *J. Phys. Chem. C* **2018**, *122*, 5040.
[157] S. V. Gaponenko, *Introduction to Nanophotonics*, Cambridge University Press, Cambridge, UK **2010**.
[158] J. Li, S. K. Cushing, P. Zheng, F. Meng, D. Chu, N. Wu, *Nat. Commun.* **2013**, *4*, 2651.
[159] R. Xu, L. Wen, Z. Wang, H. Zhao, S. Xu, Y. Mi, Y. Xu, M. Sommerfeld, Y. Fang, Y. Lei, *ACS Nano* **2017**, *11*, 7382.
[160] Y. Fang, Y. Jiao, K. Xiong, R. Ogier, Z.-J. Yang, S. Gao, A. B. Dahlin, M. Käll, *Nano Lett.* **2015**, *15*, 4059.
[161] J. Zhang, X. Jin, P. I. Morales-Guzman, X. Yu, H. Liu, H. Zhang, L. Razzari, J. P. Claverie, *ACS Nano* **2016**, *10*, 4496.
[162] J. K. Nørskov, T. Bligaard, B. Hvolbæk, F. Abild-Pedersen, I. Chorkendorff, C. H. Christensen, *Chem. Soc. Rev.* **2008**, *37*, 2163.
[163] S. Trasatti, *J. Electroanal. Chem. Interfacial Electrochem.* **1980**, *111*, 125.
[164] S. Trasatti, *J. Electroanal. Chem. Interfacial Electrochem.* **1972**, *39*, 163.
[165] A. J. Bard, A. B. Bocarsly, F. R. F. Fan, E. G. Walton, M. S. Wrighton, *J. Am. Chem. Soc.* **1980**, *102*, 3671.
[166] F. Malara, A. Minguzzi, M. Marelli, S. Morandi, R. Psaro, V. Dal Santo, A. Naldoni, *ACS Catal.* **2015**, *5*, 5292.
[167] F. Malara, F. Fabbri, M. Marelli, A. Naldoni, *ACS Catal.* **2016**, *6*, 3619.
[168] F. Le Formal, N. Tétreault, M. Cornuz, T. Moehl, M. Grätzel, K. Sivula, *Chem. Sci.* **2011**, *2*, 737.
[169] M. Haro, R. Abargues, I. Herraiz-Cardona, J. Martínez-Pastor, S. Giménez, *Electrochim. Acta* **2014**, *144*, 64.
[170] L. Wang, H. Hu, N. T. Nguyen, Y. Zhang, P. Schmuki, Y. Bi, *Nano Energy* **2017**, *35*, 171.
[171] F. F. Abdi, A. Dabirian, B. Dam, R. van de Krol, *Phys. Chem. Chem. Phys.* **2014**, *16*, 15272.
[172] M. Valenti, D. Dolat, G. Biskos, A. Schmidt-Ott, W. A. Smith, *J. Phys. Chem. C* **2015**, *119*, 2096.

[173] Y. Shi, J. Wang, C. Wang, T.-T. Zhai, W.-J. Bao, J.-J. Xu, X.-H. Xia, H.-Y. Chen, *J. Am. Chem. Soc.* **2015**, *137*, 7365.
[174] Z. Yin, B. Chen, M. Bosman, X. Cao, J. Chen, B. Zheng, H. Zhang, *Small* **2014**, *10*, 3537.
[175] G. Liu, P. Li, G. Zhao, X. Wang, J. Kong, H. Liu, H. Zhang, K. Chang, X. Meng, T. Kako, J. Ye, *J. Am. Chem. Soc.* **2016**, *138*, 9128.
[176] W. W. Gärtner, *Phys. Rev.* **1959**, *116*, 84.
[177] J. S. DuChene, G. Tagliabue, A. J. Welch, W.-H. Cheng, H. A. Atwater, *Nano Lett.* **2018**, *18*, 2545.
[178] J. Lee, S. Mubeen, X. Ji, G. D. Stucky, M. Moskovits, *Nano Lett.* **2012**, *12*, 5014.
[179] S. Mubeen, J. Lee, N. Singh, S. Krämer, G. D. Stucky, M. Moskovits, *Nat. Nanotechnol.* **2013**, *8*, 247.
[180] S. Mubeen, J. Lee, D. Liu, G. D. Stucky, M. Moskovits, *Nano Lett.* **2015**, *15*, 2132.
[181] H. Robatjazi, S. M. Bahauddin, C. Doiron, I. Thomann, *Nano Lett.* **2015**, *15*, 6155.
[182] C. Ng, J. J. Cadusch, S. Dligatch, A. Roberts, T. J. Davis, P. Mulvaney, D. E. Gómez, *ACS Nano* **2016**, *10*, 4704.